Miner Petrol (2017) 111:523–545
DOI 10.1007/s00710-017-0506-2

ORIGINAL PAPER

Differing responses of zircon, chevkinite-(Ce), monazite-(Ce) and fergusonite-(Y) to hydrothermal alteration: Evidence from the Keivy alkaline province, Kola Peninsula, Russia

Ray Macdonald[1,2] · **Bogusław Bagiński**[1] · **Dmitry Zozulya**[3]

Received: 4 August 2016 / Accepted: 14 March 2017 / Published online: 27 March 2017

Abstract A quartzolite from the Rova occurrence, Keivy alkali granite province, Kola Peninsula, Russia, is used to examine the differing responses of certain rare-metal minerals during interaction with hydrothermal fluids. The minerals are two silicates [chevkinite-(Ce) and zircon], a phosphate [monazite-(Ce)] and an oxide [fergusonite-(Y)]. Textural evidence is taken to show that the dominant alteration mechanism was interface-coupled dissolution-reprecipitation. Zircon was the most pervasively altered, possibly by broadening of cleavage planes or fractures; the other minerals were altered mainly on their rims and along cracks. The importance of cracks in promoting fluid access is stressed. The compositional effects of the alteration of each phase are documented. The hydrothermal fluids carried few ligands capable of transporting significant amounts of rare-earth elements (REE), high field strength elements (HFSE) and actinides; alteration is inferred to have been promoted by mildly alkaline, Ca-bearing fluids. Expansion cracks emanating from fergusonite-(Y) are filled with unidentified material containing up to 35 wt% UO_2 and 25 wt% REE_2O_3, indicating late-stage, short-distance mobility of these elements. Electron microprobe chemical dating of monazite yielded an age of 1665 ± 22 Ma, much younger than the formation age of the Keivy province (2.65–2.67 Ga) but comparable to that of the Svecofennian metamorphic event which affected the area (1.9–1.7 Ga) or during fluid-thermal activation of the region during rapakivi granite magmatism (1.66–1.56 Ga). Dates for altered monazite range from 2592 ± 244 Ma to 773 ± 88 Ma and reflect disturbance of the U-Th-Pb system during alteration.

Keywords Hydrothermal alteration · Zircon · Monazite · Chevkinite · Fergusonite · Quartzolite

Editorial handling: I. Broska

Electronic supplementary material The online version of this article (doi:10.1007/s00710-017-0506-2) contains supplementary material, which is available to authorized users.

✉ Ray Macdonald
r.macdonald@lancaster.ac.uk

[1] Institute of Geochemistry, Mineralogy and Petrology, University of Warsaw, 02-089 Warszawa, Poland

[2] Environment Centre, Lancaster University, Lancaster LA1 4YQ, UK

[3] Geological Institute, Kola Science Centre, Russian Academy of Sciences, Apatity, Russia

Introduction

A considerable body of research over the past three decades has shown that accessory phases containing rare-earth elements (REE), high-field-strength elements (HFSE) and actinides, such as monazite, zircon, xenotime, chevkinite and thorite, are prone to alteration during interaction with hydrothermal fluids. This has consequences for element mobility, with implications for their concentration into ore deposits and the suitability of the accessory phases for geochronological studies. Several studies have addressed the *relative* stability of accessory minerals during hydrothermal alteration. Monazite has generally been regarded as a mineral resistant to alteration on geological time-scales, which may make its use in nuclear waste disposal attractive (Lumpkin et al. 2004, 2014). Meldrum et al. (1996, 1997, 2000) reported that ABO_4-type phosphates, such as monazite ($REEPO_4$), are less susceptible to radiation damage than ABO_4-type silicates, such as zircon ($ZrSiO_4$), because its lattice repairs itself more quickly than it is destroyed, even at low temperature. However, as Lumpkin et al. (2014) acknowledged, several studies have shown that

monazite can be altered by hydrous fluids, variably enriched in F and/or CO_2, to produce, inter alia, monazite of different composition, allanite, apatite, rhabdophane, thorite, xenotime, and REE-carbonates (Poitrasson et al. 2000; Seydoux-Guillaume et al. 2002; Johan and Johan 2005; Berger et al. 2008; Hetherington and Harlov 2008; Bosse et al. 2009; Budzyń et al. 2010; Harlov and Hetherington 2010; Hetherington et al. 2010; Harlov et al. 2011; Ondrejka et al. 2012). Johan and Johan (2005) studied the interaction of magmatic zircon, thorite, xenotime and monazite with a fluid phase rich in F, CO_2 and H_2O in the Cínovec granite cupola, Czech Republic; all except the monazite were strongly hydrated and fluorinated.

Zircon has also been shown to be prone to alteration by low-temperature hydrothermal fluids, with replacement of formula elements (Zr, Si ± Hf ± Pb) by non-formula elements, such as Ca, Fe and REE (Smith et al. 1991; Geisler et al. 2003a; Pérez-Soba et al. 2007; Utsunomiya et al. 2007; Anderson et al. 2008; Nasdala et al. 2009, 2010; Van Lichtervelde et al. 2009; Lisowiec et al. 2013). The greater ease with which zircon is altered compared to the orthophosphates, such as monazite, is thought to be due to the greater strength of P-O bonds in tetrahedral coordination than Si-O bonds (Meldrum et al. 1996).

The REE-Ti-silicate chevkinite has also been shown to be altered by hydrothermal fluids (Kartashov 1994; Jiang 2006; Vlach and Gualda 2007; Bagiński et al. 2015; Macdonald et al. 2015a, b, c), the nature of the final alteration products being strongly dependent on the nature of the fluids, especially the proportions of H_2O, CO_2 and F. In many cases, the chevkinite initially alters to a Ti ± Nb ± Th-rich phase, depleted in Ca, Fe, REE and Si, the so-called "altered chevkinite", whose nature has not yet been determined.

Ercit (2005) outlined the main compositional effects of post-metamictization alteration of $YNbO_4$ minerals, namely hydration, gain of Si, Al and large ion lithophile elements (LILE), Ca addition, exchange of HREE + Y for LREE, and loss of *A*-site cations. More specifically, in their study of the recrystallization mechanisms of metamict fergusonite, Tomašíc et al. (2006) reported, in a mineral from Ytterby, Sweden, a water content of 8.12 wt% and considerable variation in *A*-site cations, especially Ca, Fe and Y. Ruschel et al. (2010) reported that during fluid-induced alteration of fergusonite from Berere, Madagascar, altered areas were generally enriched in Si and Ca and depleted in Y.

This report describes the textural and compositional features of two silicates (chevkinite-(Ce) and zircon), a phosphate (monazite-(Ce)) and an oxide (fergusonite-(Y)) which crystallized together and were subsequently altered by interaction with low-temperature fluids, in a quartzolite intrusion of the Keivy alkali granite complex, Kola Peninsula, NW Russia. Their relative stabilities during alteration are assessed, the nature of the hydrothermal fluids outlined and some of the implications for element transport considered.

Geological setting

The Keivy alkali granite complex comprises seven sheet-like masses with a total exposure area of ~2500 km^2 (Fig. 1), including the largest ones, West Keivy (1200 km^2), Ponoy (700 km^2) and White Tundra (240 km^2). The U/Pb zircon age of the granites is 2.67–2.65 Ga (Mitrofanov et al. 2000; Zozulya et al. 2005). All the rocks in the massif were metamorphosed during the Svecofennian event at 1.9–1.7 Ga (Gorbatschev and Bogdanova 1993). Numerous Zr-Y-REE-Nb ore occurrences and deposits are associated with different lithologies, including mineralised granites, quartzolites, various metasomatic rocks and pegmatites, and were formed by different petrogenetic processes (Bel'kov et al. 1988; Zozulya and Eby 2010). Attention was drawn to the Keivy quartzolites by the discovery in the Arabian Shield of the large Jabal Hamra rare-metal deposit, which is hosted in a quartzolite related to alkali granite (Drysdall et al. 1984).

The term quartzolite ("silexite" in the Russian literature; Bel'kov et al. 1988) refers in the Keivy alkaline province to bodies of variable shape, size and composition confined to the contact zone between mineralized granites and gneissic country rocks. Quartzolites occur at the apical parts of alkali granite intrusions where they are hosted by both the granites and adjoining gneisses (Fig. 1). They are thought to be transitional between early higher-temperature orthomagmatic granites and fluid-magmatic rocks like schlieren pegmatites. Diffuse transitions to silicified host granite are typical of intragranite quartzolites, whereas the contacts with gneisses are sharp and cross-cutting. Most quartzolite bodies vary from 0.5 to 1.5 m across; the largest body, from the Purnach alkali granite intrusion, reaches 40 × 40 m.

The Keivy quartzolites vary from leucocratic to mesocratic. They are inequigranular, taxitic rocks, ranging from fine-grained to pegmatitic. A distinguishing feature is the very low content of feldspar (<10 vol.%). Quartz contents range from 50 to 90 vol.%. The primary mafic rock-forming mineral is aegirine or arfvedsonite; occasionally they are present in equal amounts. Magnetite and ilmenite also frequently occur as rock-forming minerals but in lesser amounts. Sporadic large annite laths occur in some bodies. The significant amount of fluorite and other F- and OH-bearing minerals indicates active involvement of fluid in the formation of the quartzolites.

The rare-metal mineralization in the Keivy quartzolites is volumetrically significant (up to 20–30 vol.%) and variable in composition (more than ten Y, Nb, REE, Zr and Th-bearing mineral species have been recorded). Zircon is the typomorphic mineral of the ore assemblages. Other rare-metal minerals are irregularly distributed (from a few grams

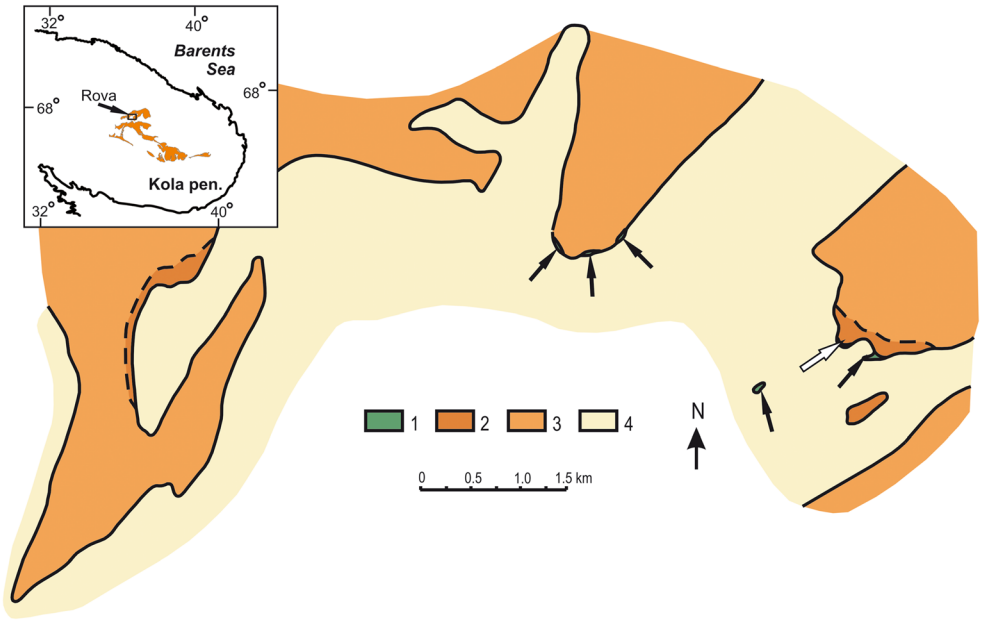

Fig. 1 Locality map showing Rova occurrence in the West Keivy massif. 1, quartzolite; 2. mineralized alkali granite; 3, alkali granite; 4, gneiss of Keivy complex; The quartzolite bodies (arrowed) are distributed mainly at the contact between mineralized granite and country rock gneisses. The quartzolite studied here is marked by a white arrow. The inset map shows the location of the Keivy alkali granite complex in the Kola Peninsula, Russia

to tens of kilograms per ton of rock) and are represented by aeschynite-(Y), chevkinite-(Ce), fergusonite-(Y), britholite-group minerals, yttrialite-(Y), thorite, monazite-(Ce), xenotime-(Y) and bastnäsite-(Ce). Fluorbritholite-(Y) and ytttrialite-(Y) are normally the main REE concentrators and their content reaches 10–15 vol.% (Lyalina et al. 2014).

This study has focussed on quartzolites from the Rova occurrence in the West Keivy massif (Fig. 1). The rocks occur as up to ten outcrops about 0.5–1.0 m in size, spread over an area of 100 × 200 m. It is not clear whether they form separate bodies or are part of a single larger mass. The quartzolites contain quartz, microcline, aegirine, arfvedsonite, magnetite, ilmenite, fluorite, zircon, fergusonite-(Y), monazite-(Ce), britholite-(Y), yttrialite-(Y), thorite, chevkinite-(Ce) and aeschynite-(Ce). It is inferred from textural relationships that quartz was the primary mineral, followed by pyroxene, amphibole and biotite. The chevkinite, fergusonite, monazite and partly the zircon are the earliest phases among the rare-metal minerals. The quartz is often brecciated and this process is accompanied by crystallization of late zircon and magnetite, britholite, yttrialite and REE carbonates. Thus the phases forming the topic of this study can all be considered primary.

The rare-metal phases occur in very different proportions, as reflected in whole-rock chemical analyses (Table 1), which also show the very high contents of many rare elements, e.g. Zr, Nb and REE. Two dominant assemblages can be recognised: (i) chevkinite-(Ce) + monazite-(Ce) + zircon + fergusonite-(Y), and (ii) yttrialite-(Y) + britholite-(Y) + zircon + thorite. The first assemblage tends to occur in adjacent

Table 1 Composition of whole-rocks

Analysis no.	1	2	3		1	2	3
Major oxides (in wt%)				Trace elements (in ppm)			
SiO_2	67.29	61.04	61.72	Rb	-	40	190
TiO_2	2.35	1.77	4.27	Sr	17	130	160
ZrO_2	6.48	0.35	1.51	La	786	2842	1912
Y2O3	0.58	2.49	1.77	Ce	2000	7240	5548
Al_2O_3	1.74	5.53	3.41	Pr	270	1085	765
Fe_2O_3	7.75	7.34	6.89	Nd	1190	4183	3440
FeO	3.31	7.64	7.70	Sm	590	1360	2752
MnO	0.13	0.36	0.68	Eu	41	157	172
MgO	0.07	0.24	0.53	Gd	920	1958	2480
CaO	1.17	2.55	1.81	Tb	190	476	1349
Na_2O	2.90	4.01	2.29	Dy	1430	3438	392
K_2O	0.56	0.88	1.67	Ho	380	793	1218
Li_2O	0.03	0.01	-	Er	800	2433	2871
P_2O_5	0.11	0.46	0.42	Tm	123	481	748
F	0.03	0.37	0.43	Yb	878	4120	3960
CO_2	0.04	0.14	0.37	Lu	27	107	88
S	0.09	0.01	-	Nb	14,300	240	60
LOI	0.85	0.64	1.16				
Sum	95.48	95.83	96.63				
O ≡ F	0.01	0.16	0.18				
Total	95.47	95.67	96.45				

LOI loss on ignition

country rocks, the second in the apical parts of granite bodies. This report concerns the first assemblage. Compositionally, it most closely resembles analysis 1 in Table 1.

Analytical techniques

The whole-rock composition was determined for major elements by atomic absorption spectrophotometry; TiO_2 by colorimetry; K_2O and Na_2O by flame photometry; FeO and CO_2 by titration; and F and Cl by potentiometry using an ion-selective electrode. Zirconium and REE were determined by X-ray fluorescence. Other trace elements were determined by Inductively Coupled Plasma-Mass Spectrometry.

Mineral compositions were determined by electron microprobe, using a Cameca SX-100 microprobe equipped with four wavelength dispersive spectrometers (WDS) and a Cameca SX Five FE equipped with five spectrometers holding large crystals. The accelerating voltage was 15 kV or 20 kV and the probe current was 20 or 40 nA. Counting times were 20 s on peak and 10 s on each of two background positions. The standards, crystals and X-ray lines used and detection limits for chevkinite are given in Bagiński et al. (2015); those for the other main phases are given here as Appendices. The 'PAP' φ(ρZ) program (Pouchou and Pichoir 1991) was used for corrections. Representative analyses are presented in Tables 2-7; the full data set is given in Supplementary Tables 1 and 2. Back scattered electron (BSE) images were made on the same equipment as the mineral analyses. Th-U-Pb ages for monazite were calculated using the methodology presented in Skridlaite et al. (2014).

Results

Textural relationships

The phases studied tend to form aggregates embedded in a quartz matrix (Fig. 2). Microcline is a minor component of the matrix but is not seen in the images presented here. Mutual contacts between the phases are sharp and occasionally one phase forms inclusions in another, such as zircon in monazite and fergusonite in chevkinite. They clearly were broadly coeval. The radially arranged cracks cutting through the quartz from the fergusonite-(Y) aggregates are probably a result of a volume increase associated with the radiation-induced amorphisation of the actinide-bearing mineral (Lumpkin et al. 2004; Gieré et al. 2009). The cracks are up to 10 μm thick and are filled with material ranging from homogeneous and bright to a patchy mix of darker and lighter components (Figs. 3a and b).

General descriptions of minerals

Chevkinite-(Ce)

The following description of the chevkinite-(Ce) expands on that presented by Bagiński et al. (2015). Crystals are deep red, euhedral to subhedral, up to 4 × 2 mm in size, and usually heavily fractured. They do not show birefringence and are isotropic when viewed under crossed polars. Several larger crystals have a brownish alteration rim up to 100 μm thick which shows as a patchy darker (lower Z) material on BSE images (Fig. 4a). The lower Z phase also penetrates along cracks into the crystals, pointing to the role of these fractures as preferential fluid flow paths, and as incipient alteration spots (Fig. 4b). In the more complex situation shown in Fig. 4c, the boundary between the main crystal and the alteration rim is irregular and thins around a fergusonite-(Y) crystal partly included in the chevkinite-(Ce). In detail (Fig. 4d), the altered area contains three subzones; that nearest the chevkinite-(Ce) (Zone B1) is lighter and less porous than the neighbouring darker subzone (B2), which grades to an outer rim (B3) comprising a brighter, highly porous, chaotic intergrowth of phases which also partly replace Zone B1. The textural variation seems to point to a multi-stage replacement of the chevkinite-(Ce).

Fergusonite-(Y)

Fergusonite-(Y) crystals are brown, heavily fractured, vary from tabular to prismatic, and are up to 2 mm across (Fig. 2). They do not show interference colours under crossed polars, indicative of a high level of structural radiation damage, as noted by Ruschel et al. (2010) in fergusonite from the Berere region, Madagascar. Analytical work has focused on three representative crystals. (1) Fergusonite 1 is a subhedral plate (350 × 265 μm) partially enclosed in chevkinite-(Ce) (Chv 1; Fig. 4c). It has a patchy, brighter core, (red-orange on Fig. 5a), rimmed by a darker material (green) of variable thickness containing small areas of the brighter component. Fergusonite 2 is a tabular crystal (320 × 240 μm) in sharp contact with Zrn1 (Figs. 2 and 5b). The crystal has a thin (≤20 μm) rim which is slightly darker on BSE images than the bright core. The third crystal is a fractured prism (550 × 90 μm) situated close to the chevkinite-(Ce) in Fig. 4c. It has the same backscattering coefficient as the rims of the other two crystals, with residual patches of brighter material towards its core.

Zircon

Zircon forms euhedral crystals with rectangular sections up to 0.5 mm across, normally associated with chevkinite-(Ce) or fergusonite-(Y) (Fig. 2). Some show patchy, faint interference

Table 2 Representative compositions of unaltered and altered chevkinite

Analysis no.	1	2	3	4	5	6	7	8	9
Major oxides (in wt%)									
P_2O_5	0.08	b.d.l.	0.04	0.05	0.03	b.d.l.	b.d.l.	b.d.l.	b.d.l.
Nb_2O_5	1.00	1.06	1.04	1.44	1.75	1.92	3.00	2.43	2.33
Ta_2O_5	0.17	0.14	0.16	0.20	0.12	0.10	b.d.l.	0.10	0.19
SiO_2	18.56	18.60	18.67	16.38	11.26	10.69	9.61	8.82	22.28
TiO_2	16.02	16.25	15.85	16.90	25.57	23.34	24.10	21.36	26.46
ZrO_2	bd	0.07	b.d.l.	b.d.l.	b.d.l.	0.11	b.d.l.	0.19	0.07
ThO_2	1.98	1.94	2.22	2.12	2.89	3.38	4.13	3.70	2.28
UO_2	0.09	0.17	b.d.l.	0.22	0.23	0.58	1.20	1.19	0.31
Al_2O_3	0.05	0.09	0.08	0.63	1.74	1.95	1.83	1.91	0.43
Y_2O_3	1.43	1.38	1.28	1.14	1.05	0.99	0.90	0.97	4.09
La_2O_3	9.01	8.73	9.06	6.96	2.06	1.91	1.65	1.65	4.17
Ce_2O_3	20.31	19.41	19.79	18.05	18.82	16.28	13.52	13.07	11.27
Pr_2O_3	2.41	2.28	2.19	2.00	0.89	0.60	0.48	0.58	1.29
Nd_2O_3	9.14	7.64	7.27	6.00	2.68	2.46	3.49	1.88	4.09
Sm_2O_3	1.65	1.39	1.50	1.11	0.79	0.67	0.58	0.68	1.15
Gd_2O_3	1.15	1.25	1.08	0.76	0.66	0.73	0.93	0.67	1.41
Dy_2O_3	0.61	0.68	0.58	0.50	0.80	0.54	b.d.l.	0.77	1.12
CaO	1.41	1.41	1.32	0.84	0.04	0.10	0.04	b.d.l.	4.47
MnO	0.33	0.40	0.35	0.23	b.d.l.	0.06	b.d.l.	b.d.l.	0.35
FeO*	11.94	12.12	12.49	10.35	3.90	3.42	3.29	3.04	4.07
SrO	b.d.l.	0.13	0.18	0.07	b.d.l.	0.04	b.d.l.	b.d.l.	0.13
BaO	0.14	0.13	b.d.l.	b.d.l.	0.17	b.d.l.	b.d.l.	b.d.l.	0.27
Total	97.48	95.27	95.15	85.95	75.45	69.87	68.75	63.01	92.23
Mineral formulae on basis of 22 oxygens per formula unit (in a.p.f.u.)									
Ca	0.330	0.333	0.313	0.215	0.011	0.029	0.012	0.000	0.922
Sr	0.000	0.017	0.023	0.010	0.000	0.006	0.000	0.000	0.015
Ba	0.012	0.011	0.000	0.000	0.017	0.000	0.000	0.000	0.020
La	0.726	0.710	0.739	0.613	0.194	0.192	0.169	0.186	0.296
Ce	1.625	1.566	1.601	1.577	1.756	1.629	1.374	1.459	0.794
Pr	0.192	0.183	0.176	0.174	0.083	0.060	0.049	0.064	0.090
Nd	0.713	0.601	0.574	0.511	0.244	0.240	0.346	0.205	0.281
Sm	0.124	0.106	0.114	0.091	0.069	0.063	0.055	0.071	0.076
Gd	0.083	0.091	0.079	0.060	0.056	0.066	0.086	0.068	0.090
Dy	0.043	0.048	0.041	0.038	0.066	0.048	0.000	0.076	0.069
Y	0.166	0.162	0.151	0.145	0.142	0.144	0.133	0.157	0.419
Th	0.098	0.097	0.112	0.115	0.168	0.210	0.261	0.257	0.100
U	0.004	0.008	0.000	0.012	0.013	0.035	0.074	0.081	0.013
Sum *A*	4.117	3.934	3.923	3.561	2.818	2.723	2.559	2.624	3.187
Fe^{2+}	1.000	1.000	1.000	1.000	0.831	0.781	0.764	0.775	0.655
Mn	0.000	0.000	0.000	0.000	0.000	0.014	0.000	0.000	0.057
Sum *B*	1.000	1.000	1.000	1.000	0.831	0.795	0.764	0.775	0.712
Fe^{2+}	1.181	1.234	1.308	1.066	0.000	0.000	0.000	0.000	0.000
Mn	0.061	0.075	0.066	0.046	0.000	0.000	0.000	0.000	0.057
Zr	0.000	0.008	0.000	0.000	0.000	0.015	0.000	0.028	0.007
Nb	0.099	0.106	0.104	0.155	0.202	0.237	0.377	0.335	0.203
Ta	0.010	0.008	0.010	0.013	0.008	0.007	0.000	0.008	0.010
Al	0.013	0.023	0.021	0.177	0.523	0.628	0.599	0.686	0.098
Ti	0.632	0.693	0.634	1.033	2.901	2.796	3.031	2.898	1.830

Table 2 (continued)

Analysis no.	1	2	3	4	5	6	7	8	9
Sum *C*	1.996	2.147	2.142	2.491	3.633	3.683	4.006	3.956	2.204
Ti (= *D*)	2.000	2.000	2.000	2.000	2.000	2.000	2.000	2.000	2.000
Si	4.054	4.099	4.126	3.909	2.869	2.921	2.668	2.689	4.289
P	0.015	0.000	0.007	0.010	0.006	0.000	0.000	0.000	0.000
Sum *T*	4.069	4.099	4.133	3.919	2.876	2.921	2.668	2.689	4.289
Σ cations	13.18	13.18	13.20	12.97	12.16	12.12	12.00	12.05	12.39

Explanation: analyses 1–3, 4–6, 7–9 from Zones A, B1, B2 in chevkinite-(Ce) shown in Fig. 4d

FeO*, all Fe as Fe^{2+}

b.d.l., below detection limit

Data from Bagiński et al. (2015)

a.p.f.u., atoms per formula unit

colours. Crystals comprise two components of different intensity (different Z) on BSE images; textural relationships point to a virtually complete replacement of the lighter by the darker component. The progressive replacement is shown in Fig. 6; in Figs. 6a and b there are approximately equal amounts of lighter and darker components and the boundaries between them are sharp. In Figs. 6c and d, the darker component is extremely patchy and the boundaries between the components are commonly marked by a thin dark rim. A compositional profile has been made along the line marked P1 in Fig. 6c. Rounded to irregular dark areas are more common in the dark component. It is not easy to determine whether they are pore spaces or holes made during preparation of the section but the very small round holes are taken to be pores. Small, bright inclusions of an unidentified Nb-oxide phase (marked as NbO? on Fig. 6a) tend to be more common in the darker component and in "residual islands" of the brighter component. Other inclusions include monazite-(Ce), $ThSiO_4$, albite and K-feldspar.

Monazite-(Ce)

Monazite-(Ce) is light-grey and forms mainly equant crystals ~1 mm across but also occurs as prisms up to 1.5 mm long

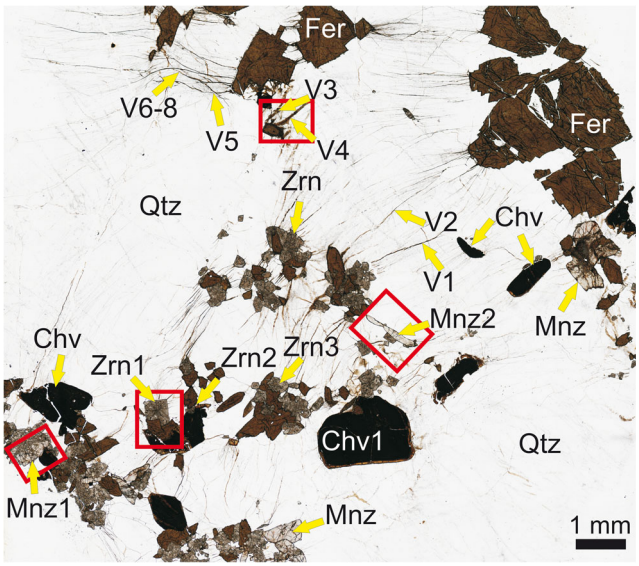

Fig. 2 Photomicrograph (plane polarized light) of quartzolite, to show textural relationships. The numbered crystals have been the focus of the electron microprobe determinations. Chevkinite-(Ce) (Chv), monazite-(Ce) (Mnz), zircon (Zrn) and fergusonite-(Y) (Fer) tend to occur in clusters within a quartz (Qtz) matrix. Expansion cracks, such as veinlets V1 to V8, have formed radially around the clusters, especially where fergusonite-(Y) is present

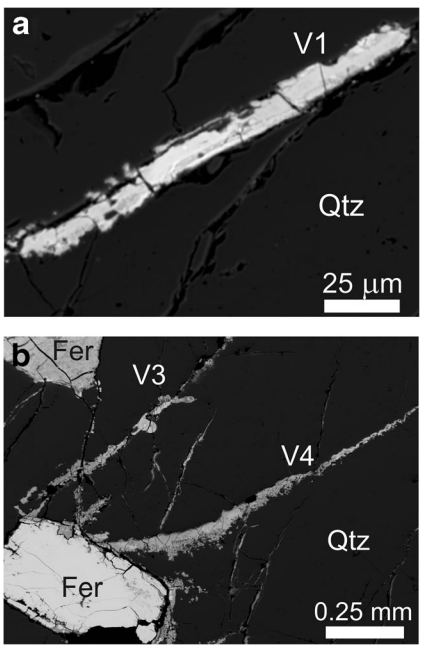

Fig. 3 BSE images of veinlets infilling expansion cracks cutting quartz (Qtz). Their locations are shown on Fig. 2. **a** Patchily zoned, relatively bright type. Veinlet 1. **b** Veinlet 3, showing variable thickness, form and intensity along its length, and Veinlet 4, fairly homogeneous grey near the fergusonite-(Y) (Fer) and becoming patchy and brighter towards its tip

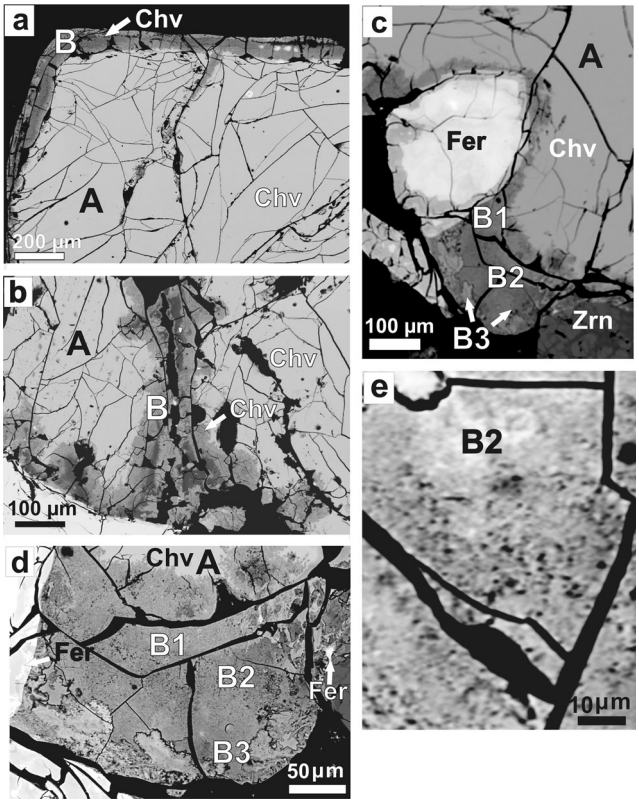

Fig. 4 BSE images of textural relationships in chevkinite-(Ce) (Fig. 2, Chv1). **a** Fractured chevkinite-(Ce) (A) has dark rim of altered chevkinite (B), with some residual patches of unaltered material (e.g. in top right). The darker component extends up the large fracture in the centre of the image. **b** More extensive alteration along a fracture. The darkest component tends to be more central within the fracture. **c** The alteration rim thins around the associated, patchily zoned fergusonite-(Y) (Fer) crystal and then **d** to the right, thickens into three complex alteration subzones (B1, B2, B3) which are mixes of several regions of different intensity. Subzones B2 and B3 are highly porous (Fig. 4e). A prismatic fergusonite-(Y) on the bottom left in Fig. 4c contains remnants of the bright core material. See also Bagiński et al. (2015)

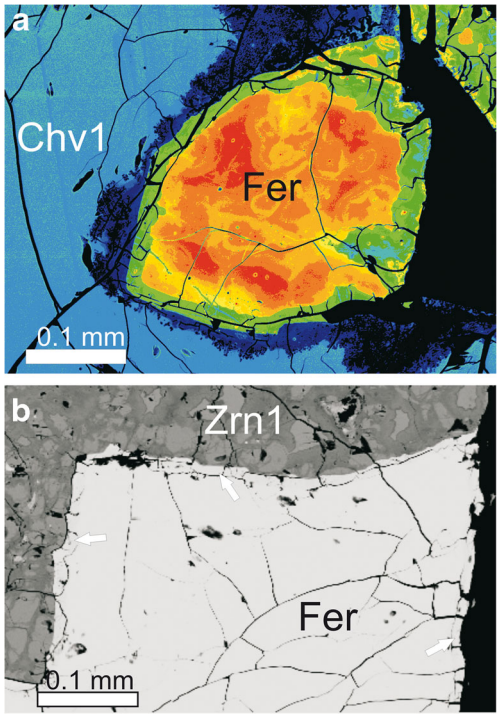

Fig. 5 **a** False colour BSE image of subhedral fergusonite-(Y) (Fer) crystal associated with Chv1 (Figs. 2 and 4c). A patchy core (orange) is mantled by a rim (green) of variable thickness which includes patches of the core material. The small crystal at top right is a more completely altered fergusonite-(Y). Altered chevkinite is *dark blue* to *black*. **b** Fergusonite-(Y) intergrown with Zrn1 (Fig. 2). The rim of the fergusonite-(Y), marked by arrows, is slightly darker than the core. Details of the zircon texture are shown in Fig. 6

(Fig. 2). It is less heavily fractured than the fergusonite-(Y) and shows bright interference colours, suggesting low levels of radiation damage. Zonation, seen as areas of different intensity on BSE images, is common. In crystal Mnz2 (where Mnz means monazite), areas of different intensity are randomly intergrown, with some strips of a higher Z phase (Figs. 7a and b). The boundaries between the different components tend to be sharp. Fractures cross, and clearly post-date, the zones.

Certain crystals show a rather different type of zonation on BSE images; for example, the crystal (Mnz1) in Figs.7c and d consists mainly of monazite (mon A) showing slightly different BSE intensities, here termed light and grey. The boundaries between them tend to be sharp. The crystal also shows areas of lower Z (mon B, dark) occurring along fractures. These areas contain small anhedral inclusions of $ThSiO_4$, seen as bright spots of very variable size. Larger cracks around the dark area are the result of sample preparation.

Mineral compositions

Chevkinite-(Ce)

Chevkinite and perrierite, the two most common minerals of the chevkinite-group of minerals (CGM), have the general formula $A_4BC_2D_2(Si_2O_7)_2O_8$, where the dominant cations in each site are: *A*, REE^{3+}, Ca^{2+}; *B*, Fe^{2+}; *C*, Fe^{2+}, Fe^{3+}, Ti^{4+}, Al^{3+}; *D*, Ti^{4+}. EPMA of the unaltered chevkinite-(Ce) in the quartzolite may be found in Macdonald et al. (2012) and Bagiński et al. (2015); compositions representative of three of the zones shown in Fig. 4 are given in Table 2. The phase has been classified as chevkinite using the empirical discriminant of Macdonald et al. (2009). There are relatively high ThO_2 (2.1 wt%) and Nb_2O_5 (1.1 wt%) contents. Uranium levels are below detection (~770 ppm). During alteration, loss of LREE led to a deficiency in the *A* site; there was also a significant loss of Fe and a loss of Si. In contrast, there was enrichment in Ti (maximum total Ti = 5.4 apfu), Nb, Th and Al.

On a chondrite-normalized plot (Fig. 8a), the unaltered chevkinite-(Ce) shows strong LREE enrichment while the altered phase shows positive Ce anomalies.

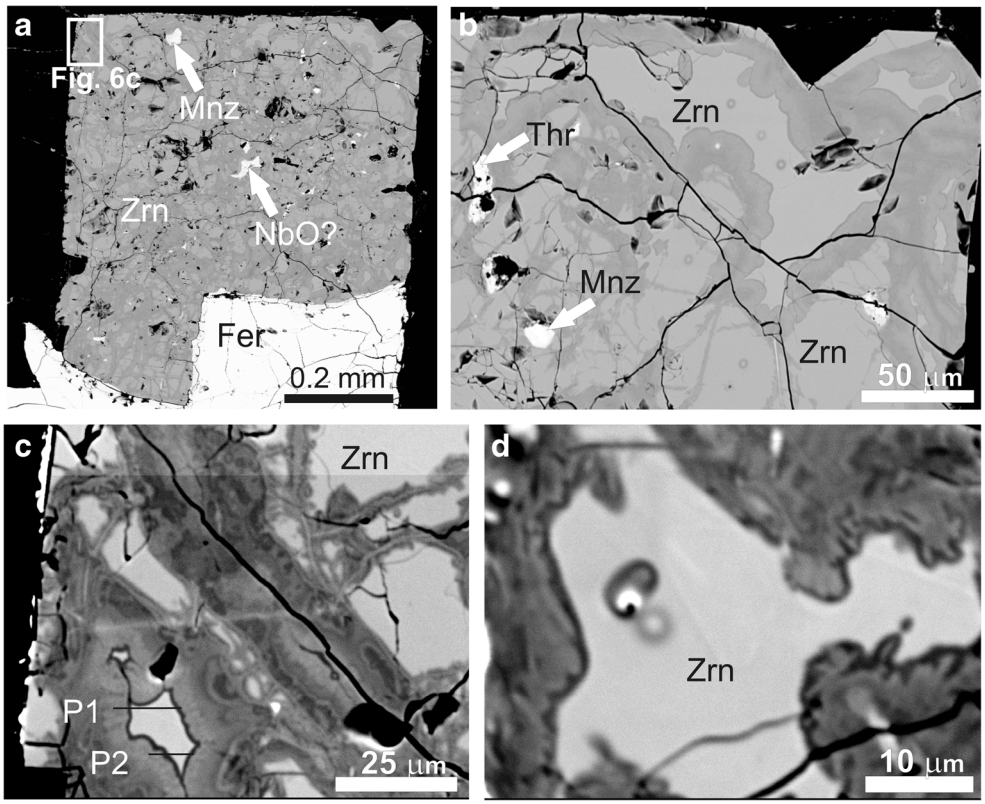

Fig. 6 Progressive replacement of the lighter component by a darker component in Zrn1 (Fig. 2). **a, b** Random pattern of replacement of lighter by darker component. The boundaries between the components are sharp. In Figs 6**c** and **d**, the darker component is very patchy, with residual islets of lighter component. The mutual boundaries are still relatively sharp, although in some cases are marked by a thin dark rim (e.g. at P1 and P2). The rounded areas in the light component at centre left (Fig. 6d) are a result of beam damage. Note the bright inclusions of monazite-(Ce), (Mnz) an unidentified Nb-oxide phase (NbO?) and $ThSiO_4$ (Thr). Line P1 in Fig. 6c marks the WDS profile shown in Fig. 10

Fergusonite-(Y)

Analytical work on fergusonite-(Y) focused on the three crystals described above in the Textural Relationships section; representative analyses are given in Table 3; the full data set is in Supplementary Table 1a. Classification has been made using the three-group canonical discriminant of Ercit (2005; Fig. 9). Fergusonite has the structural

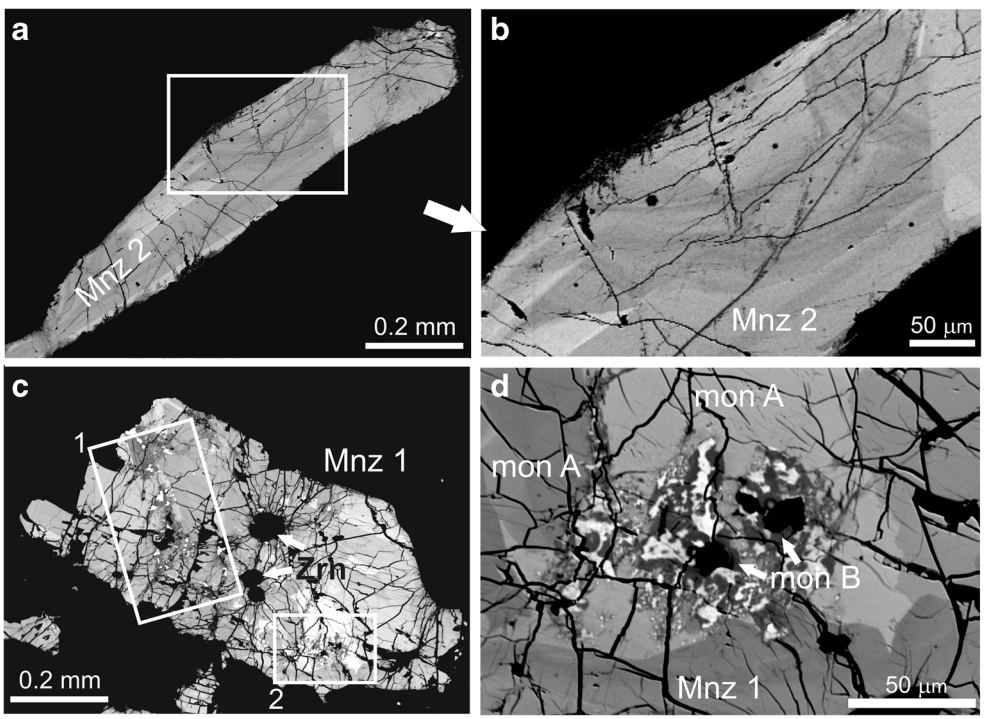

Fig. 7 BSE images of monazite-(Ce). **a** Crystal Mnz2 (Fig. 2) shows irregular zonation of several components of different intensity. The brightest phase forms both a partial rim and internal strips. **b** Details of the zonation in Mnz2. **c** Heavily fractured monazite-(Ce) (crystal Mnz1, Fig. 2). The dominant component (mon A) is lighter to darker grey but it has been patchily and irregularly replaced by a much darker component (mon B). The darkest regions contain bright, anhedral grains of $ThSiO_4$, which are most abundant in the outlined areas, marked as rectangles 1 and 2. The black euhedral inclusions are zircon (Zrn). **d** Detail of $ThSiO_4$-bearing area (part of the field marked as rectangle 2 in 7c)

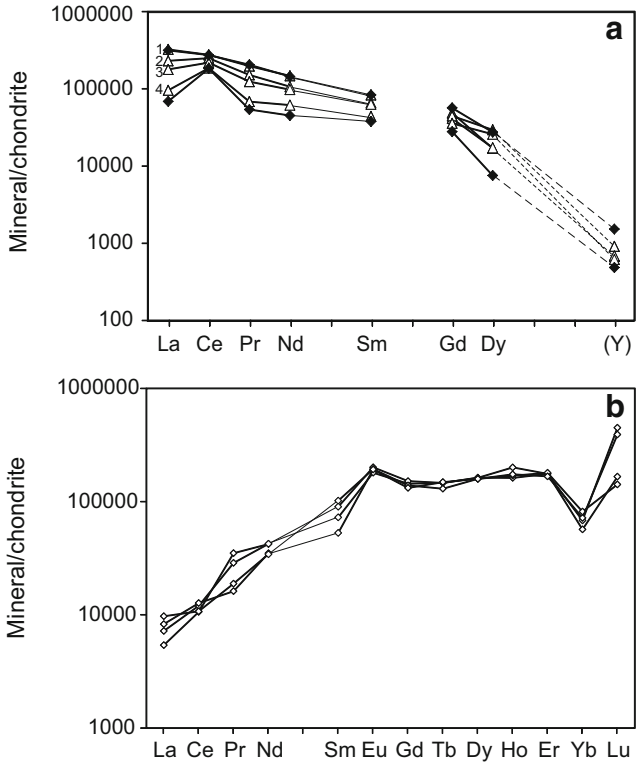

Fig. 8 Chondrite-normalized REE patterns for chevkinite and fergusonite. **a** Chevkinite-(Ce) (1; average of 17 analyses) and altered chevkinite (2, Subzone B1 (8); 3, Subzone B2 (10), 4, Subzone B3 (6)). See Fig. 4c. Data from Macdonald et al. (2012) and Bagiński et al. (2015). The compositional spread within Subzones B1-B3 is exemplified by the range for B1 (limited by heavier lines and filled symbols). **b** The fergusonite-(Y) patterns are variable but all are HREE-enriched, with significant positive Eu anomalies. Data from Supplementary Table 1a, numbers 2, 9, 4 and 3. Normalizing factors from Sun and McDonough (1989)

formula $A^{3+}B^{5+}O_4$, where the *A* site is dominated by the REE, especially Y, and the *B* site by Nb. All other cations have been allocated to the *A* site. Fe has been calculated as Fe^{3+} (e.g. Ervanne 2004). The *A* site is occupied mainly by Y (0.45–0.53 apfu), with significant amounts of the other REE (Σ0.27–0.36 apfu). Thorium, U, Ca and Fe are generally present at levels <0.1 apfu. Niobium dominates the *B* site (0.78–0.95 apfu), with low levels of Ta (<0.01 apfu) and Nb/(Nb + Ta) atomic ratios exceeding 0.99.

A chondrite-normalised plot (Fig. 8b) shows that the fergusonite-(Y) is LREE-depleted and HREE + Y-enriched. There are significant positive Eu anomalies, Eu/Eu* 1.6–2.4. The persistent negative anomaly at Yb has not, so far as we know, been previously recorded in fergusonite (e.g. Gieré et al. 2009; Uher et al. 2009; Ruschel et al. 2010; Prol-Ledesma et al. 2012) and may be related to multiple overlaps in the spectra, artificially increasing Lu values (see also Appendix for fergusonite analytical conditions).

Table 3 Representative compositions of fergusonite-(Y)

Analysis no.	1	2	3	4	5	6	7
Major oxides (in wt%)							
WO_3	0.22	0.17	0.13	0.09	0.53	0.11	0.17
P_2O_5	0.03	0.03	0.03	0.02	b.d.l.	0.07	b.d.l.
Nb_2O_5	43.99	43.48	43.23	38.78	38.61	43.84	40.53
Ta_2O_5	0.45	0.41	0.47	0.49	0.55	0.45	0.36
SiO_2	0.09	0.18	1.43	5.74	6.71	0.12	4.19
TiO_2	1.72	1.70	1.73	1.62	1.57	1.93	1.64
ZrO_2	b.d.l.	b.d.l.	b.d.l.	b.d.l.	b.d.l.	b.d.l.	b.d.l.
ThO_2	2.24	2.70	2.20	1.88	1.92	3.61	2.02
UO_2	3.54	3.56	3.55	3.10	2.95	3.60	3.43
Al_2O_3	b.d.l.	b.d.l.	b.d.l.	0.02	b.d.l.	b.d.l.	b.d.l.
Fe_2O_3*	1.00	0.99	1.12	1.68	1.63	0.21	1.36
Y_2O_3	20.82	20.10	19.87	19.76	18.90	20.26	19.45
La_2O_3	0.16	0.11	0.23	0.27	0.58	0.17	0.24
Ce_2O_3	0.70	0.76	0.71	0.77	1.58	0.85	0.84
Pr_2O_3	0.33	0.39	0.32	0.21	0.38	0.21	0.22
Nd_2O_3	2.28	2.26	2.01	1.87	1.97	2.63	2.08
Sm_2O_3	1.80	1.71	1.56	0.94	1.41	1.92	1.39
Eu_2O_3	1.36	1.19	1.41	1.29	1.09	1.41	1.27
Gd_2O_3	3.58	3.46	3.48	3.13	3.24	3.72	3.29
Tb_2O_3	0.61	0.60	0.62	0.64	0.65	0.63	0.65
Dy_2O_3	5.22	5.15	4.86	4.63	4.30	5.10	4.61
Ho_2O_3	1.24	1.26	1.14	1.13	1.25	1.01	1.31
Tm_2O_3	0.45	0.32	0.49	b.d.l.	b.d.l.	0.37	0.36
Er_2O_3	3.45	3.32	3.31	3.16	3.22	3.37	3.33
Yb_2O_3	1.49	1.36	1.35	1.39	1.36	1.24	1.49
Lu_2O_3	0.35	0.62	0.48	1.13	0.58	0.37	0.54
CaO	1.22	1.47	1.89	2.08	2.34	0.37	2.11
MnO	0.05	0.11	0.08	0.12	b.d.l.	0.06	0.11
PbO	b.d.l.	0.04	0.08	0.52	b.d.l.	0.36	0.13
Total	98.39	97.45	97.78	96.46	97.32	97.99	97.12
Mineral formulae on the basis of (Nb + Ta + Ti + W) = 1 per formula unit (a.p.f.u.)							
Ca	0.061	0.075	0.096	0.118	0.133	0.019	0.115
La	0.003	0.002	0.004	0.005	0.011	0.003	0.004
Ce	0.012	0.013	0.012	0.015	0.031	0.015	0.016
Pr	0.006	0.007	0.006	0.004	0.007	0.004	0.004
Nd	0.038	0.038	0.034	0.035	0.037	0.044	0.038
Sm	0.029	0.028	0.026	0.017	0.026	0.031	0.024
Eu	0.022	0.019	0.023	0.023	0.020	0.022	0.022
Gd	0.056	0.054	0.055	0.055	0.057	0.058	0.055
Tb	0.009	0.009	0.010	0.011	0.011	0.010	0.011
Dy	0.079	0.079	0.075	0.079	0.073	0.077	0.075
Ho	0.018	0.019	0.017	0.019	0.021	0.015	0.021
Tm	0.007	0.005	0.007	0.000	0.000	0.005	0.006
Er	0.051	0.049	0.050	0.053	0.054	0.049	0.053
Yb	0.021	0.020	0.020	0.022	0.022	0.018	0.023
Lu	0.005	0.009	0.007	0.018	0.009	0.005	0.008
Y	0.519	0.508	0.504	0.556	0.533	0.504	0.526

Table 3 (continued)

Analysis no.	1	2	3	4	5	6	7
Zr	0.000	0.000	0.000	0.000	0.000	0.000	0.000
Th	0.024	0.029	0.024	0.023	0.023	0.038	0.023
U	0.037	0.038	0.038	0.037	0.035	0.037	0.039
Fe^{3+}	0.035	0.035	0.040	0.067	0.065	0.007	0.052
Mn	0.002	0.004	0.003	0.005	0.000	0.002	0.005
Pb	0.000	0.001	0.001	0.007	0.000	0.005	0.002
Si	0.004	0.009	0.068	0.304	0.356	0.006	0.213
Al	0.000	0.000	0.000	0.001	0.000	0.000	0.000
P	0.001	0.001	0.001	0.001	0.000	0.003	0.000
A cations	1.039	1.051	1.120	1.476	1.525	0.976	1.336
Nb	0.932	0.933	0.931	0.928	0.925	0.926	0.931
Ta	0.006	0.005	0.006	0.007	0.008	0.006	0.005
Ti	0.061	0.061	0.062	0.064	0.063	0.068	0.063
W	0.001	0.001	0.001	0.001	0.004	0.001	0.001
B cations	1.000	1.000	1.000	1.000	1.000	1.000	1.000
Σ cations	2.04	2.05	2.12	2.48	2.52	1.98	2.34

Explanation: 1–5, core to rim profile through subhedral plate (Fig. 5a); 6, core of crystal intergrown with zircon (Fig. 5b); 7, anhedral prism (Fig. 4c)

Fe_2O_3*, all Fe as Fe^{3+}

b.d.l., below detection limit

a.p.f.u., atoms per formula unit

Zircon

A euhedral rectangular plate associated with fergusonite-(Y) (Zrn 1, Fig. 5b) and three smaller crystals are compositionally representative of the zircon (Table 4 and Supplementary Table 1b). The higher BSE intensity component has oxide totals in the range 99.08–99.94 wt% and is close to stoichiometric ($Zr_{0.99}Si_{0.99}O_{4.0}$). Thorium levels are below the limit of detection (~700 ppm). Uranium oxide abundances range up to 0.15 wt%. Phosphorus levels are low (< 0.01 apfu) and Ca, Ti, Al, Fe, Sc and the LREE are below detection limits. The Zr/Hf ratios are high, 78–105; the average value is 90.

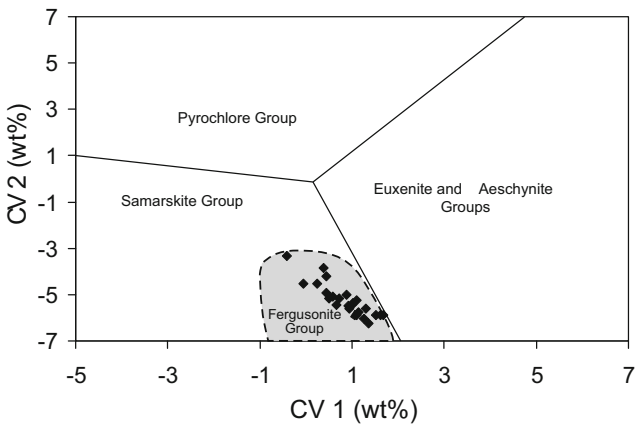

Fig. 9 Fergusonite-(Y) plotted as canonical variables CV1 and CV2 of the three-group model of Ercit (2005). Data from Supplementary Table 1a. CV1 = 0.245 Na + 0.106 Ca – 0.077 Fe* + 0.425 Pb + 0.220 Y + 0.280 LREE +0.137 HREE +0.100 U* + 0.304 Ti + 0.097 Nb + 0.109 Ta* -12.81 (oxide wt%). CV2 = 0.102 Na – 0.113 Ca – 0.371 Fe* - 0.167 Pb – 0.395 Y – 0.265 HREE – 0.182 U* - 0.085 Ti – 0.166 Nb – 0.146 Ta* + 17.29 (oxide wt%). Fe* = Fe + Mn; U* = U + Th; Ta* = Ta + W

The darker component has lower Si, Zr and Hf and higher Ca, Fe, P and (with one exception) U and Y abundances, than the brighter component (Table 4). Aluminium and Ti are detectable in two point analyses. One point analysis, in Zrn2, has detectable levels of LREE (0.56 wt% La_2O_3, 1.2 wt% Ce_2O_3 and 0.21 wt% Nd_2O_3; Supplementary Table 1b, anal. 25). The oxide analytical totals are low (93.5–97.0 wt%) and the cation sums slightly too high (2.06–2.08 apfu, as compared to the ideal value of 2.00 apfu). Hafnium levels are slightly lower (average 0.98 wt% HfO_2) than in the brighter phase (1.3 wt%) and Zr/Hf ratios are generally higher, 102–106 (average 103).

Elemental line scans for Ca, Fe, U, Y and Zr (Fig. 10) were made along a line crossing the dark rim of a residual zircon (P1, Fig. 6c). Zirconium levels are slightly lower in the altered phase but Ca levels increase very sharply over a distance of ~1 μm. It is unclear why the rims should be so dark on the BSE images, one possibility being the presence of undetected nanoporosity (Ruschel et al. 2010).

Monazite-(Ce) and $ThSiO_4$

Two monazite crystals showing textural differences (Fig. 7) were analysed in some detail. Representative analyses are given in Table 5 and the full data set is in Supplementary Tables 1c and 2. The discussion of compositional variations is divided into two sections: (i) the main areas of crystals Mnz1 and Mnz2; and (ii) the dark phase associated with fractures in Mnz1.

The terms Mnz1 etc. refer to the numbered crystals as shown in Fig. 2.

The analytical totals in crystals Mnz2 and the brighter areas of Mnz1 (mon A) are in the range 96.7–99.5 wt% (average 98.1 wt%). The cation sums, based on four oxygens, are 1.99–2.01 apfu (average 2.00 apfu). Thorium levels are high (≤21.7 wt% ThO_2); U levels are ≤0.66 wt% (~0.01 apfu) and the Th/U atomic ratio ranges from 25 to 53 (average 35). The phase is virtually free of Ca (≤0.01 apfu) and most Fe and Mn determinations were below detection limits. Lead values range from 0.001–0.017 apfu and are positively correlated with Th. The most variable component is ThO_2 (10.67–21.7 wt%), while Ce_2O_3 ranges from 22.0–27.1 wt% and P_2O_5 from 20.7–25.6 wt%. Silicon abundances are relatively high, up to 0.22 apfu. Chondrite-normalised REE patterns show strong LREE enrichment and little fractionation among the LREE, e.g. $[La/Sm]_{CN}$ (where CN is chondrite-

Table 4 Representative compositions of zircon

Analysis no.	1 Unaltered	2	3	4	5	6 Altered	7	8	9	10
Major oxides (in wt%)										
P_2O_5	0.20	0.09	0.11	0.06	b.d.l.	0.09	0.49	0.18	0.13	0.27
SiO_2	31.77	31.76	32.15	32.28	32.32	30.49	29.52	29.71	30.54	30.64
TiO_2	b.d.l.	b.d.l.	0.04	b.d.l.	b.d.l.	1.29	b.d.l.	0.03	b.d.l.	b.d.l.
ZrO_2	65.32	66.71	65.53	66.30	65.73	61.05	60.68	56.32	56.91	57.13
HfO_2	1.12	1.09	1.13	1.27	1.26	1.07	1.01	0.94	0.94	0.95
UO_2	0.56	0.11	0.13	0.11	b.d.l.	0.23	0.53	0.53	0.45	0.72
Al_2O_3	b.d.l.	b.d.l.	b.d.l.	b.d.l.	b.d.l.	b.d.l.	0.50	0.58	b.d.l.	b.d.l.
Y_2O_3	0.43	0.04	0.05	b.d.l.	b.d.l.	0.07	0.50	0.58	0.51	0.81
Yb_2O_3	0.20	0.18	b.d.l.	b.d.l.	b.d.l.	b.d.l.	0.16	b.d.l.	b.d.l.	b.d.l.
CaO	b.d.l.	b.d.l.	b.d.l.	b.d.l.	b.d.l.	1.68	2.23	2.60	2.43	2.36
FeO*	b.d.l.	b.d.l.	b.d.l.	0.08	0.06	1.29	1.39	2.08	2.05	1.65
PbO	b.d.l.	b.d.l.	b.d.l.	b.d.l.	b.d.l.	b.d.l.	b.d.l.	b.d.l.	b.d.l.	0.29
Total	99.60	99.98	99.14	100.10	99.37	97.26	97.01	93.55	93.96	94.82
Mineral formulae on the basis of 4 oxygens per formula unit (a.p.f.u.)										
Zr	0.988	1.005	0.989	0.993	0.990	0.943	0.947	0.904	0.908	0.906
Hf	0.010	0.010	0.010	0.011	0.011	0.010	0.009	0.009	0.009	0.009
U	0.004	0.001	0.001	0.001	0.000	0.002	0.004	0.004	0.003	0.005
Ti	0.000	0.000	0.001	0.000	0.000	0.031	0.000	0.001	0.000	0.000
Y	0.007	0.000	0.001	0.000	0.000	0.001	0.009	0.010	0.009	0.014
Yb	0.002	0.002	0.000	0.000	0.000	0.000	0.002	0.000	0.000	0.000
Ca	0.000	0.000	0.000	0.000	0.000	0.057	0.076	0.092	0.085	0.082
Fe^{2+}	0.000	0.000	0.000	0.002	0.002	0.034	0.037	0.057	0.056	0.045
Al	0.000	0.000	0.000	0.000	0.000	0.000	0.019	0.022	0.000	0.000
Si	0.985	0.981	0.995	0.992	0.998	0.966	0.945	0.978	0.999	0.996
P	0.005	0.002	0.003	0.002	0.000	0.002	0.013	0.005	0.004	0.007
cations	2.00	2.00	2.00	2.00	2.00	2.05	2.06	2.08	2.07	2.07

Sample descriptions: 1, 2, 3, 6, 7, 8 - in zircon 1; 4, 9 - in zircon 3; 5, 10 - in monazite 1. Locations of crystals in Fig. 2

Values of Z fall from left to right

FeO*, all Fe as Fe^{2+}

b.d.l., below detection limit

a.p.f.u., atoms per formula unit

normalized) varies only from 4.8–6.0, but more fractionation between LREE and HREE (e.g. $[La/Y]_{CN}$ from 95 to 124) (Fig. 11). Cerium anomalies are moderate and negative (Ce/Ce* 0.78–0.81; Supplementary Table 2). There are positive correlations between Th, U and Si, balanced by decreases in total REE, Y and P (and increasing degrees of intensity), indicating the presence of a huttonite substitution mechanism (Fig. 12), to a maximum of about 25% huttonite component (Watt 1995; Förster 1998).

The dark areas in Mnz1 (mon B) have markedly lower ThO_2 abundances (down to 2.9 wt%), lower U, P and Si, and higher REE, P and Y contents. The sharp drop in Th content is related to the formation of $ThSiO_4$, which is concentrated as irregular inclusions in the dark zones (Figs. 7c, d). The total REE content of the monazite increased during alteration but the LREE were not significantly fractionated by the process (Fig. 11; Supplementary Table 2). $[La/Y]_{CN}$ ratios are generally higher and show a wider range (72–612) than in the pristine phase. Among the heavier REE, the dark monazite with $ThSiO_4$ inclusions shows relative Gd enrichment and stronger Y depletion than the other types.

Representative compositions of $ThSiO_4$ are given in Table 6. Notable features include the high levels of P_2O_5 (≤9.8 wt%) and $LREE_2O_3$ (≤26.9 wt%), features typical of compositional modification during hydrothermal alteration. REE distribution in the $ThSiO_4$ is more variable than in the monazite: $[La/Nd]_{CN}$ ranges from 1.3–4.4 whilst $[La/Y]_{CN}$ ranges from 2 to 101. With two exceptions, the analyses show small positive Ce anomalies (Ce/Ce* ≤1.5) (Fig. 11).

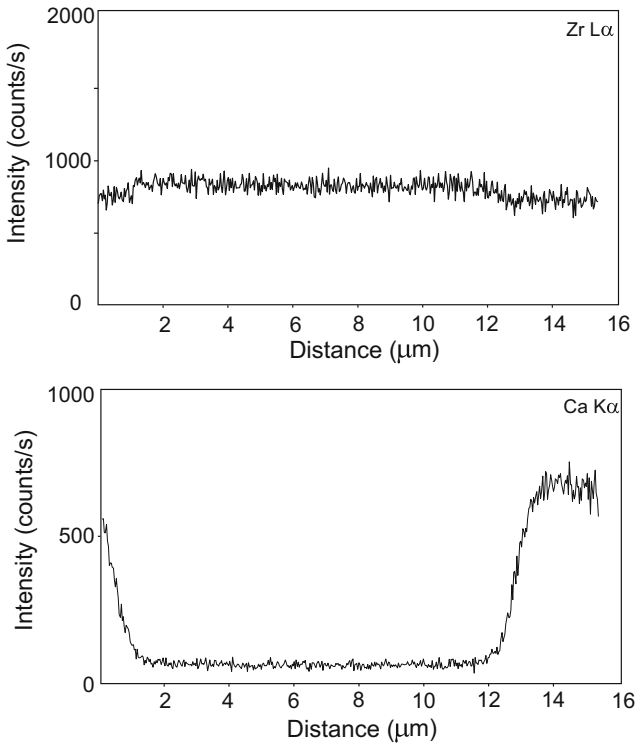

Fig. 10 WDS line scans of zircon along the profile P1 shown in Fig. 6c. The formula elements (exemplified by Zr) show a small drop in abundance over the thin dark rim, whereas the non-formula elements (e.g. Ca) show rapid increases (over a distance of ~1 μm)

Expansion cracks in quartz

Compositions of the material filling the expansion cracks in quartz (Figs. 2 and 3) are presented in Table 7. All are dominated by Nb, U, Pb and REE, with lesser amounts of Th, Si and Fe. Two main types can be distinguished: the first is rich in U (up to 35 wt% UO_2), the second in REE (≤25 wt% REE_2O_3). Abundances of PbO are up to 27 wt%, whereas ThO_2 levels are <0.7 wt%, with one exception (6 wt%). Silicon and Fe are highest in the REE-rich type. Chlorine levels are low (≤0.18 wt%) and F levels are below detection. Chondrite-normalised REE patterns are rather flat, with $[La/Yb]_{CN}$ varying from 1.5–4.3, and with strong Ce enrichment relative to the other LREE (Ce/Ce* 1.0–5.6). Analytical totals are low (75–90 wt%). The nature of the vein-filling material is uncertain. Compositionally it has some similarities to altered members of the pyrochlore supergroup but it may not be crystalline. The veins do, however, provide evidence of fluid mobility during or after the alteration of the fergusonite-(Y).

Chemical dating of monazite alteration

Detailed electron microprobe analyses were made of monazite-(Ce) in two areas of crystal Mnz1, marked 1 and 2 on Fig. 7c, which comprise lighter (mon A) and darker (mon B) components, the latter with $ThSiO_4$ inclusions. Two levels of BSE intensity were distinguished in the lighter (mon A) areas, light and grey (Fig. 7c). Compositional data for these two areas are given separately in Supplementary Table 2. However, they are compositionally so similar that, for dating purposes, they are here treated together. Compared to the lighter domains, the dark areas (mon B) show a wider compositional spread and are lower in Th, U, Pb, Si, Dy and Y but higher in LREE (Table 7), as noted above for the fuller data set.

Th-U-Pb ages for the lighter areas (mon A) range from 1737 ± 101 Ma to 1582 ± 133 Ma, with an average of 1665 ± 22 Ma (Fig. 13). The age range in the darker component (mon B) is from 2592 ± 244 Ma to 773 ± 88 Ma, with an average of 1908 ± 180 Ma.

Discussion

Compositional variations related to hydrothermal alteration

As noted above, the darker component in the chevkinite lost Ca and Fe relative to the lighter component. In contrast, there was enrichment in Ti, Nb, Th and Al. These changes are typical of the alteration of chevkinite by hydrothermal fluids (Bagiński et al. 2015). Following Jiang (2006) and Vlach and Gualda (2007), Bagiński et al. (2015) termed similar phases "altered chevkinite" but they clearly do not fit the standard CGM formula. No information is available on its structural state. Alteration of the chevkinite-(Ce) resulted in the loss of La relative to the other LREE and of the LREE relative to the HREE (Fig. 8a). A small positive Ce anomaly in the unaltered phase (Ce/Ce* 1.1) increased on average to 1.3 during alteration.

Compositional variations within the fergusonite-(Y) are linked to textural position within crystals. From bright cores to dark rims (Figs. 5a and b), there are increases in Ca, La, Ce, W, Fe, Pb and Si contents and decreases in Y, Nb and REE from Pr-Gd. The analytical totals decrease to 92.28 wt% and the sums of cations increase to 2.08 apfu. Ruschel et al. (2010) reported broadly comparable chemical alteration patterns in fergusonite from the Berer region, Madagascar, namely enrichment in Si and Ca and depletion in Y, and also related the changes to interaction with fluids. The entry of Si into the structure might explain the unusually high Si values in some point analyses in the quartzolite (up to 0.26 apfu; 5.7 wt% SiO_2). Even higher values (≤9.4 wt% SiO_2) were recorded by Ruschel et al. (2010).

The compositional differences between the two domains in zircon, along with the lower BSE intensity and the presence of porosity, are compatible with the darker component

Table 5 Representative compositions of monazite-(Ce)

Crystal	Mnz1							Mnz2		
Analysis no.	1	2	3	4	5	6	7	8	9	10
Major oxides (in wt%)										
P_2O_5	22.28	20.71	23.20	24.83	27.10	27.25	28.40	21.28	22.65	24.96
SiO_2	4.40	5.73	3.82	3.06	1.48	1.72	0.89	5.18	3.84	2.86
ThO_2	16.49	21.66	13.54	11.27	5.55	6.05	2.99	19.86	14.30	10.79
UO_2	0.51	0.66	0.36	0.26	b.d.l.	0.13	b.d.l.	0.57	0.51	0.25
Y_2O_3	0.82	0.84	1.00	0.82	0.61	0.70	0.59	0.87	0.77	0.79
La_2O_3	12.33	11.00	12.65	13.96	14.83	14.30	15.63	11.01	13.00	13.95
Ce_2O_3	24.30	22.01	25.04	26.84	28.93	28.00	29.76	22.73	24.99	26.90
Pr_2O_3	2.33	2.61	2.77	2.84	2.74	3.05	3.40	2.54	2.74	2.83
Nd_2O_3	10.32	9.25	10.74	11.53	11.84	11.59	11.95	10.46	10.33	11.03
Sm_2O_3	1.46	1.51	1.52	1.56	1.69	1.98	1.94	1.50	1.50	1.71
Gd_2O_3	0.85	1.16	1.09	0.96	1.11	2.96	2.94	0.97	0.88	0.89
Dy_2O_3	b.d.l.	b.d.l.	0.50	0.37	0.36	b.d.l.	b.d.l.	0.51	b.d.l.	0.41
Ho_2O_3	0.22	0.23	0.30	0.16	0.40	b.d.l.	b.d.l.	b.d.l.	0.43	b.d.l.
Yb_2O_3	0.03	0.13	0.12	b.d.l.	0.25	0.26	b.d.l.	b.d.l.	b.d.l.	b.d.l.
CaO	0.09	0.02	0.04	0.09	0.04	0.07	b.d.l.	0.04	0.05	0.07
MnO	b.d.l.	b.d.l.	0.05	0.02	0.03	b.d.l.	b.d.l.	b.d.l.	b.d.l.	b.d.l.
FeO*	b.d.l.	b.d.l.	b.d.l.	0.04	0.06	b.d.l.	b.d.l.	b.d.l.	b.d.l.	b.d.l.
PbO	1.10	1.21	0.89	0.49	0.13	b.d.l.	b.d.l.	1.51	0.92	0.47
F	b.d.l.	b.d.l.	b.d.l.	b.d.l.	b.d.l.	0.38	0.33	b.d.l.	b.d.l.	b.d.l.
Sum	97.53	98.73	97.63	99.10	97.15	98.44	98.82	99.03	96.91	97.91
O = F	0.00	0.00	0.00	0.00	0.00	0.16	0.14	0.00	0.00	0.00
Total	97.53	98.73	97.63	99.10	97.15	98.28	98.68	99.03	96.91	97.91
Mineral formulae on basis of 4 oxygens per formula unit (a.p.f.u.)										
Ca	0.004	0.001	0.002	0.004	0.002	0.003	0.000	0.002	0.002	0.003
La	0.195	0.175	0.198	0.213	0.224	0.213	0.231	0.174	0.206	0.214
Ce	0.381	0.348	0.389	0.406	0.434	0.415	0.436	0.357	0.394	0.410
Pr	0.036	0.041	0.043	0.043	0.041	0.045	0.050	0.040	0.043	0.043
Nd	0.158	0.142	0.163	0.170	0.173	0.167	0.171	0.160	0.159	0.164
Sm	0.022	0.022	0.022	0.022	0.024	0.028	0.027	0.022	0.022	0.025
Gd	0.012	0.017	0.015	0.013	0.015	0.040	0.039	0.014	0.013	0.012
Dy	0.001	0.000	0.007	0.005	0.005	0.000	0.000	0.007	0.000	0.005
Ho	0.003	0.003	0.004	0.002	0.005	0.000	0.000	0.000	0.006	0.000
Yb	0.000	0.000	0.000	0.000	0.003	0.003	0.000	0.000	0.000	0.000
Y	0.019	0.019	0.023	0.018	0.013	0.015	0.013	0.020	0.018	0.017
Th	0.161	0.213	0.131	0.106	0.052	0.056	0.027	0.194	0.140	0.102
U	0.005	0.006	0.003	0.002	0.000	0.001	0.000	0.005	0.005	0.002
Fe^{2+}	0.000	0.000	0.000	0.001	0.002	0.000	0.000	0.000	0.000	0.000
Mn	0.000	0.000	0.002	0.000	0.000	0.000	0.000	0.000	0.000	0.000
Pb	0.013	0.014	0.010	0.005	0.001	0.000	0.000	0.017	0.011	0.005
Si	0.189	0.247	0.162	0.126	0.061	0.070	0.036	0.222	0.165	0.119
P	0.808	0.756	0.834	0.868	0.940	0.933	0.962	0.773	0.825	0.879
F	0.031	0.023	0.024	0.024	0.029	0.049	0.042	0.023	0.025	0.025
Σ cations	2.01	2.00	2.01	2.01	1.99	1.99	1.99	2.01	2.01	2.00

Intensity on BSE images decreases from left to right within each crystal

FeO*, all Fe as Fe^{2+}

b.d.l., below detection limit, a.p.f.u., atoms per formula unit

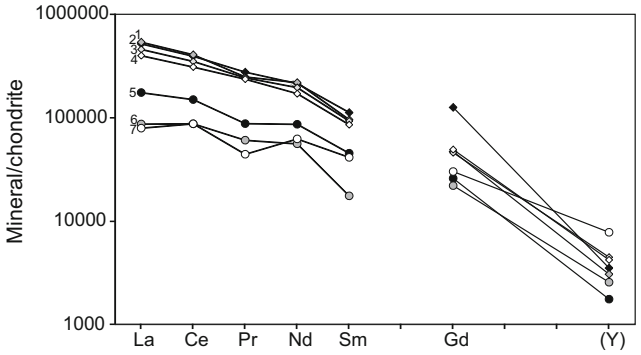

Fig. 11 Chondrite-normalized REE patterns for monazite-(Ce) and $ThSiO_4$ inclusions. All from crystal Mnz2 (Fig. 2). *Monazite-(Ce).* Patterns selected to show the compositional range based on BSE intensity; 1, dark (mon B), associated with $ThSiO_4$; 2, darker mon A; 3, 4, brighter mon A. Data from Supplementary Table 1c. *$ThSiO_4$.* Patterns 5, 6, 7. Inclusions associated with mon B. Data from Table 6. Normalizing factors from Sun and McDonough (1989)

representing hydrothermally altered zircon, with some replacement of Si, Zr and Hf by Ca, Fe, P and Y. These compositional features are very similar to those recorded in altered zircons by Smith et al. (1991), Geisler et al. (2003a), Pérez-Soba et al. (2007), Utsunomiya et al. (2007), Nasdala et al. (2009, 2010), Van Lichtervelde et al. (2009) and Lisowiec et al. (2013). Despite the textural variability, the maximum total of elements other than the major components is only 0.16 apfu, i.e. the zircon was not strongly altered compositionally. Uranium was not removed during alteration; rather, it was concentrated in the dark component, both absolutely and relative to Si and Zr. Retention of U in altered zircon has previously been recorded by Geisler et al. (2003b) and Nasdala et al. (2010).

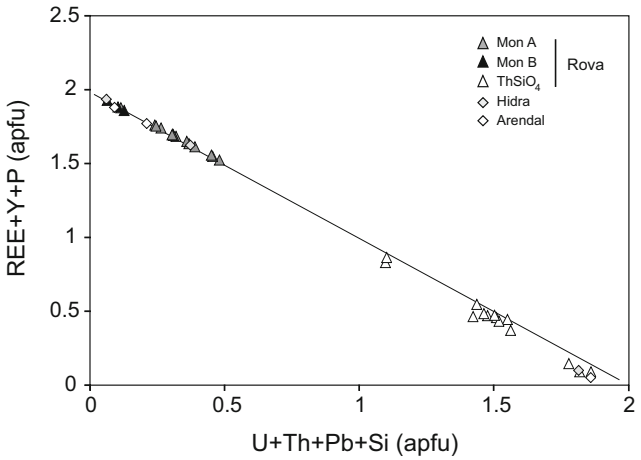

Fig. 12 (U + Pb + Th + Si) versus (REE + Y + P) plot for monazite and $ThSiO_4$ inclusions. Data for mon A lie on a linear trend between mon B and thorite, indicating that the $ThSiO_4$ formed during alteration of mon A. Rova data from Supplementary Tables 1c and 2 and Table 5, Hidra data from Hetherington and Harlov (2008) and Arendal data from Seydoux-Guillaume et al. (2012)

Table 6 Representative compositions of $ThSiO_4$

Analysis no.	1	2	3	4	5	6
Major oxides (in wt%)						
P_2O_5	0.55	5.58	4.28	3.89	5.44	9.79
SiO_2	20.38	14.90	11.15	17.89	16.00	13.59
ThO_2	62.05	51.85	51.17	48.39	57.12	41.72
UO_2	2.57	1.35	1.51	1.38	1.99	1.03
Y_2O_3	0.95	0.24	0.38	1.61	0.38	0.45
La_2O_3	0.70	2.34	2.88	2.37	2.47	6.33
Ce_2O_3	1.11	5.74	6.87	6.57	6.18	14.03
Pr_2O_3	bd	0.45	0.78	0.73	0.60	1.08
Nd_2O_3	0.31	2.40	2.84	3.63	3.19	4.67
Sm_2O_3	b.d.l.	b.d.l.	0.46	0.59	0.61	0.78
Gd_2O_3	b.d.l.	b.d.l.	b.d.l.	b.d.l.	0.67	b.d.l.
CaO	2.49	2.56	0.96	1.41	1.60	1.50
PbO	0.30	0.35	0.61	bd	0.43	0.20
Total	91.41	87.76	83.89	88.46	96.68	95.17
Mineral formulae on basis of 4 oxygens per formula unit (a.p.f.u.)						
Si	1.054	0.782	0.687	0.920	0.792	0.641
Th	0.731	0.620	0.718	0.567	0.643	0.448
U	0.030	0.016	0.021	0.016	0.022	0.011
Pb	0.004	0.005	0.010	0.000	0.006	0.003
P	0.024	0.248	0.223	0.169	0.228	0.391
Ca	0.138	0.144	0.063	0.078	0.085	0.076
La	0.013	0.045	0.065	0.045	0.045	0.109
Ce	0.021	0.110	0.155	0.124	0.112	0.242
Pr	0.000	0.009	0.018	0.014	0.011	0.019
Nd	0.006	0.045	0.063	0.067	0.056	0.079
Sm	0.000	0.000	0.010	0.010	0.010	0.013
Gd	0.000	0.000	0.000	0.000	0.011	0.000
Y	0.026	0.007	0.012	0.044	0.010	0.011
Σ cations	2.05	2.03	2.05	2.05	2.03	2.04

b.d.l., below detection limit

a.p.f.u., atoms per formula unit

The relationships in Fig. 12 indicate that the alteration of the monazite-(Ce) was of the type monazite A → monazite B + thorite (Broska et al. 2000; Harlov et al. 2007; Rasmussen and Muhling 2007; Seydoux-Guillaume et al. 2007, 2012; Hetherington and Harlov 2008). The $ThSiO_4$ in the Keivy quartzolite is, however, richer in REE + Y (≤0.47 apfu) than in the earlier studies. Importantly in terms of element mobility, the Th released during monazite breakdown was not removed from the local reaction zone (c.f. Budzyń et al. 2010, Budzyń et al. 2011). The dark, altered, monazite (mon B) has higher Th/U ratios than the primary monazite, due to a fractionation of U relative to Th during alteration, as noted by Seydoux-Guillaume et al. (2012) for monazite and thorite inclusions. Such behaviour contrasts with that in zircon, where U was retained during alteration.

Table 7 Composition of vein material in expansion cracks cutting quartz

Veinlet no.	1	2	2	3	4	5	5	7	8
Major oxides (in wt%)									
P_2O_5	0.17	0.07	0.03	b.d.l.	b.d.l.	0.06	0.04	0.04	0.07
Nb_2O_5	26.35	19.75	23.32	34.39	30.45	28.95	26.73	26.16	24.86
Ta_2O_5	0.05	0.05	b.d.l.	0.54	0.43	0.18	0.05	b.d.l.	0.06
SiO_2	4.73	4.94	2.51	6.73	5.53	4.71	3.54	2.35	2.80
TiO_2	0.51	0.52	0.57	1.15	1.21	0.47	0.56	0.30	0.48
ZrO_2	0.68	1.13	1.00	1.91	1.47	0.09	0.08	b.d.l.	b.d.l.
ThO_2	b.d.l.	0.66	0.47	5.98	0.32	b.d.l.	b.d.l.	b.d.l.	b.d.l.
UO_2	1.43	27.55	34.91	2.43	1.87	1.59	27.33	31.10	28.01
Al_2O_3	0.97	0.87	0.63	1.43	0.96	0.86	0.84	0.65	0.64
Y_2O_3	2.06	0.62	0.61	2.31	2.21	1.82	0.79	0.86	0.86
La_2O_3	0.95	0.32	0.41	1.02	0.92	0.77	0.48	0.44	0.56
Ce_2O_3	16.14	1.26	1.26	2.14	3.32	5.99	1.63	1.57	1.54
Pr_2O_3	0.53	0.13	0.16	0.25	0.24	0.16	b.d.l.	b.d.l.	b.d.l.
Nd_2O_3	1.87	0.60	0.66	1.90	1.80	1.57	0.88	0.90	0.89
Sm_2O_3	0.42	b.d.l.	b.d.l.	0.51	0.54	0.20	0.26	0.25	0.09
Gd_2O_3	1.05	0.26	0.34	1.26	1.25	0.78	0.50	0.31	0.50
Dy_2O_3	1.29	0.33	0.46	1.38	1.58	1.12	0.58	0.57	0.36
Ho_2O_3	b.d.l.	b.d.l.	b.d.l.	0.28	0.20	b.d.l.	0.20	b.d.l.	b.d.l.
Yb_2O_3	0.33	0.11	0.11	0.44	0.41	0.26	b.d.l.	0.21	0.09
Lu_2O_3	b.d.l.	b.d.l.	0.28	0.15	0.22	b.d.l.	b.d.l.	b.d.l.	b.d.l.
CaO	0.15	0.15	0.03	0.21	0.14	0.17	0.11	0.06	0.11
MnO	b.d.l.	0.03	b.d.l.	0.08	0.04	0.04	b.d.l.	b.d.l.	b.d.l.
FeO*	3.35	1.26	1.10	2.41	1.84	3.11	1.12	0.86	0.93
BaO	b.d.l.	0.37	0.29	0.10	0.09	0.05	0.05	b.d.l.	0.16
PbO	14.68	13.25	14.99	20.69	17.48	16.55	26.73	26.16	24.86
Na_2O	0.02	0.10	b.d.l.	b.d.l.	b.d.l.	0.09	0.06	b.d.l.	b.d.l.
Cl	0.13	0.18	0.17	b.d.l.	0.08	0.16	0.13	0.15	0.14
Total	77.86	74.51	84.31	89.69	74.60	69.75	92.69	92.94	88.01

FeO*, all Fe as Fe^{2+}

F, Hf, Mg and Tb all below detection limit (b.d.l.)

Alteration mechanisms: Dissolution-reprecipitation

In interface-coupled dissolution-reprecipitation, an alteration front moves into the crystal, the process being operative at the inwardly migrating reaction interface. The original mineral dissolves congruently, components being released stoichiometrically and concentrated in the fluid until saturation is reached and a new phase is precipitated onto the dissolving phase. Boundaries between the original and new phases are typically sharp (Harlov and Hetherington 2010). Fluid infiltration is promoted by the development of porosity or nano-porosity (Harlov et al. 2005; Harlov and Hetherington 2010). In the Keivy case, this may have been the process responsible for forming the alteration rims on chevkinite-(Ce) and fergusonite-(Y). If so, the outcome was rather different; whereas the fergusonite rim still has a recognizably fergusonite composition, the chevkinite rim is compositionally very different to the unaltered mineral and is probably amorphous. A dissolution-reprecipitation mechanism, involving the dissolving of monazite A and its

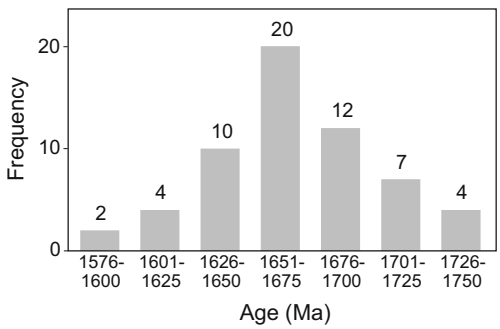

Fig. 13 Histogram of chemical dates for lighter (unaltered; mon A) zones in Mnz1. Data from Supplementary Table 2

reprecipitation as monazite B, was proposed by Hetherington and Harlov (2008) and Seydoux-Guillaume et al. (2012). Perhaps a similar mechanism was responsible for the alteration of zircon, at least during the initial stages.

Importance of cracks

The importance of cracks in promoting alteration is shown in the monazite-(Ce). We propose that alteration generally proceeded in the manner suggested by Seydoux-Guillaume et al. (2012) for monazite with $ThSiO_4$ inclusions from Norway and Madagascar. The Th-rich monazite became unstable in contact with the fluids gaining access along the cracks and dissolved. The fluid became supersaturated and precipitated the new monazite and thorite. In chevkinite-(Ce) and, to a lesser extent fergusonite-(Y), the alteration also proceeded with maximum efficiency where cracks were available; continued fluid migration along these pathways progressively altered the isolated regions.

The alteration of the zircon may have proceeded rather differently. That the crystal retained its euhedral form during alteration means that element transfers into the crystals were matched by element losses. It is possible that the crystal was replaced by a broadening of cleavage planes or fractures until regions of the original zircon were isolated, in the manner suggested for the alteration of monazite by Harlov et al. (2007). Alternatively, fluid ingress may initially have been into zones radiation-damaged during metamictisation. A weak negative correlation between Si and U may point to the increasing effects of radiation damage with increasing U content (c.f. Van Lichtervelde et al. 2009). Continued fluid migration along these pathways progressively altered the isolated regions and obscured the original fluid pathways. Fluid ingress was accompanied by the incorporation of elements such as Ca, Fe and Al.

Relative stabilities of phases during alteration

The question arises as to why the phases have different alteration patterns, considering that they interacted with the same fluids. Except along cracks, the monazite-(Ce) appears to have been relatively stable, despite its high actinide content (≤22 wt% ThO_2; ≤0.66 wt% UO_2). This may simply have been due to its structure being able to recrystallize more readily than the silicates and oxide (Meldrum et al. 1996, 1997, 2000). Zircon is almost totally altered and fergusonite-(Y) less thoroughly altered. It is not simply an effect of metamictization; the fergusonite-(Y) has the higher content of actinides (ThO_2 3.6 wt%, UO_2 3.6 wt%) and might be expected to have been the most damaged structurally and more prone to fluid influx. Alternatively, zircon has been shown to undergo increases in diffusion-based hydrothermal alteration rates due to two factors: (i) amorphous domains connect in clusters in the structure, and (ii) strongly overlapping α–recoil events form nano-sized regions of altered material which form fast diffusion pathways (Geisler et al. 2003b). Such amorphous domains may be represented by the dark zones in the Keivy minerals (Fig. 6).

Despite the complexity of its composition and structure, the chevkinite-(Ce) was significantly altered only along cracks (Fig. 4). However, the mineral is known to be heavily altered to complex new assemblages in the presence of F- and CO_2-rich fluids (Bagiński et al. 2016; Macdonald et al. 2015b, c); we ascribe its relative stability in the quartzolite to the scarcity of hard ligands in the fluids.

A somewhat arbitrary sequence of ease of alteration, for the inferred set of conditions, especially the fluid composition, and assuming that they were altered at the same time, is zircon > fergusonite > chevkinite > monazite.

Nature of hydrothermal fluids

The mineral assemblages may be used to give some indication of which ligands were present in the fluids involved in the hydrothermal alteration of the quartzolite. However, there are no carbonates (for CO_3^{2-}) or barite (for SO_4^{2-}) and the minor amounts of Cl in the expansion veinlets (≤0.18 wt%) are the only indication of the presence of Cl^-. Fluorine and CO_2 concentrations in the quartzolite are highly variable (Table 1) but in the study material fluorine-and carbonate-bearing phases are absent. The relative paucity of ligands, especially F^- and CO_3^{2-}, may also have limited the ability of the hydrothermal fluids to transport the REE and HFSE and it is noticeable that no new minerals were formed during alteration, with the exception of $ThSiO_4$ which grew by exsolution in the monazite, and possibly the unresolved material in the expansion cracks.

Certain lines of evidence suggest that the hydrothermal fluids had low alkalinity. First, Hetherington et al. (2010) showed that during alteration of monazite A by low alkalinity fluids, the assemblage monazite B + thorite forms rather than Th-rich monazite. Second, monazite alters easily in alkaline solutions (Hetherington et al. 2010), whereas most of the monazite in this study has been relatively stable (Figs 7a and b). In contrast, Ca has been significantly added to the zircon during alteration, suggesting a modest Ca content in the fluids. Furthermore, dissolution-reprecipitation has been shown experimentally to be most efficient in alkaline solutions (Harlov et al. 2011; Hetherington et al. 2010). It may be speculated, therefore, that the alteration was promoted by mildly alkaline, Ca-bearing fluids.

The presumably late-stage fluids which filled the expansion cracks are problematic. Fluorine and chlorine levels are below or close to detection limits and there are no carbonates or phosphates. Some parts are REE-rich, others Nb-rich; both parts can also be U-rich. Whatever the nature of the fluid, they clearly originated in the fergusonite-(Y) clusters (Fig. 2). Gieré et al. (2009) suggested that fergusonite is able to retain actinides even when entirely metamict; in the Keivy example, U was clearly able to be mobilized in the late hydrothermal fluids. Although the distribution of the cracks in three-dimensions is not known, it appears that the transport was limited in scale.

There is no direct evidence as to the redox conditions in the fluids. There are positive Ce anomalies in the fergusonite-(Ce) (Ce/Ce* = 2.0, 2.4) and in the altered chevkinite (average Ce/Ce* 1.3), which may have been related to elevated fO_2 conditions during interaction with fluids (Berger et al. 2008). However, other explanations may be relevant for the anomalies, such as preferential partitioning of Ce into the fluids as Ce^{4+}.

Positive Eu anomalies may have been a result of increasing oxidation. An alternative explanation comes from the study of the Tatyana pegmatite, Haldzan Buragtag massif, Mongolian Altai, by Kartashov et al. (1993), where they found very late-formed REE-bearing epidote extremely enriched in Eu. They explained the feature by liberation of Eu during albitization of host basic rocks during the main metasomatising event; the Eu went into solutions poor in REE and concentrated in the crystallizing epidote. Such a process may have been applicable to the Eu-rich fergusonite-(Y) in the quartzolite.

If uranium were present as U^{6+} in zircon, as might be expected in a strongly oxidising environment, it should have been mobilised as a result of its higher mobility than U^{4+} or U^{5+}. This might suggest that the alteration of the zircon, which retained U during alteration, did not take place under such oxidising conditions (Ruschel et al. 2010). However, it may not simply have been a redox effect, but caused by a lack of complexing anions in the fluid, such as CO_3^{2-}, F^- and Cl^- (Geisler et al. 2003a).

Significance of Th-Pb-U age determinations

The age determined for the pristine monazite-(Ce), 1665 ± 22 Ma (Fig. 13), is clearly much younger than the age of formation of the Keivy alkaline province (2670–2650 Ma; Mitrofanov et al. 2000; Zozulya et al. 2005). It is, however, more similar to the age of the regressive stage of the Svecofennian metamorphic event which affected the province at 1.9–1.7 Ga (Gorbatschev and Bogdanova 1993). More precisely, it may be related to the extensional intracratonic regimes recorded in monazites (Skridlaite et al. 2014). Otherwise, there was voluminous rapakivi granite magmatism at 1.66–1.56 Ga, occurring in the south Fennoscandian shield (Baltybayev et al. 2009; Rämö and Haapala 1995), pointing to possible fluid-thermal activation of the whole shield (and Keivy province) during that time. It appears possible that the monazite has recorded the resetting of its age during that event. U/Pb ages ranging from 1673 to 1695 Ma were also obtained for xenotime, zircon and monazite from pegmatites related to Keivy alkali granites (Bayanova and Voloshin 1999; Bayanova 2004).

The large range of ages in the altered zones of the Keivy monazite, some older than the pristine monazite, is clearly due to the considerable loss of Th, and also U and Pb (Table 8), and thus disturbance of the U-Pb system, during alteration. The ages are thus meaningless. Similar results, where altered monazite yielded ages older (or younger) than the pristine phases, were recorded by Williams et al. (2011) in monazite from a sand deposit in North Carolina and by Seydoux-Guillaume et al. (2012) in monazite from Ambato, Madagascar.

Table 8 Summary of compositional data used in chemical dating

BSE intensity	light/grey		dark	
n	40		48	
	range	average	range	average
Major oxides (in wt%)				
P_2O_5	23.00–25.59	24.42	23.57–31.52	27.96
SiO_2	3.42–5.59	4.31	0.66–4.54	1.93
ThO_2	10.67–17.96	13.31	1.46–13.87	6.05
UO_2	0.25–0.47	0.34	0.03–0.93	0.14
Y_2O_3	0.76–0.90	0.81	0.20–1.43	0.71
La_2O_3	11.47–13.88	13.06	12.29–17.04	14.71
Ce_2O_3	23.44–27.07	25.74	25.12–31.76	29.03
Pr_2O_3	2.51–2.94	2.80	2.62–3.41	3.09
Nd_2O_3	9.88–11.25	10.71	10.20–12.93	12.01
Sm_2O_3	1.43–1.59	1.50	1.31–1.84	1.68
Gd_2O_3	0.81–1.01	0.90	0.63–1.16	1.00
Dy_2O_3	b.d.l.-0.48	0.32	0.07–0.52	0.32
CaO	0.04–0.09	0.06	0.01–0.84	0.12
PbO	0.85–1.42	1.07	0.10–0.57	0.47

Full data set given in Supplementary Table 2

n - number of analyses used in averages

b.d.l., below detection limit

Acknowledgements This paper is dedicated to Dr. Piotr Dzierżanowski, who died on 31st December, 2015. His warm personality and EPMA expertise will be sorely missed by the mineralogical community. We thank Pavel Uher and Silvio Vlach for very helpful journal reviews and Igor Broska for editorial handling. Research support was provided by the Russian Foundation for Basic Research, grant nos. 16-05-00427 and 16-05-00367 to DZ, and by the National Science Centre (NCN) of Poland, grant N N307 634040 to RM and BB.

Appendices

Table 9 Analytical conditions for fergusonite

Element	Line	Crystal	Standard	Approx. detection limit (wt.%)
Al	Kα	TAP	orthoclase	0.02
Ca	Kα	PET	$CaSiO_3$	0.03
Ce	Lα	PET	CeP_5O_{14}	0.05
Dy	Lß	LIF	REE1	0.38
Er	Lα	LIF	ErP_5O_{14}	0.12
Eu	Lß	LIF	REE2	0.34
Fe	Kα	LIF	hematite	0.04
Gd	Lα	LIF	GdP_5O_{14}	0.12
Ho	Lß	LIF	HoP_5O_{14}	0.22
La	Lα	PET	LaB_6	0.05
Lu	Lα	LIF	REE4	0.33*
Mn	Kα	LIF	rhodonite	0.04
Nb	Lα	PET	Nb metal	0.06
Nd	Lß	LIF	NdP_5O_{14}	0.17
P	Kα	PET	apatite	0.03
Pb	Mα	PET	$PbCrO_4$	0.18
Pr	Lß	LIF	PrP_5O_{14}	0.21
Si	Kα	TAP	wollastonite	0.01
Sm	Lα	LIF	SmP_5O_{14}	0.10
Ta	Mα	TAP	Ta metal	0.04
Tb	Lα	LIF	REE4	0.11
Th	Mα	PET	ThO_2 synthetic	0.09
Ti	Kα	PET	rutile	0.02
Tm	Lα	LIF	TmPO4	0.14
U	Mß	PET	vorlanite	0.09
W	Mß	TAP	$CaWO_4$	0.07
Y	Lα	TAP	$Y_3Al_5O_{12}$	0.03
Yb	Lα	LIF	REE3	0.13
Zr	Lα	PET	zircon	0.05

Table 10 Analytical conditions for zircon

Element	Line	Crystal	Standard	Approx. detection limit (wt.%)
Al	Kα	TAP	orthoclase	0.01
Ca	Lα	PET	$CaSiO_3$	0.01
Fe	Kα	LiF	hematite	0.03
Hf	Mα	TAP	HfO_2	0.03
P	Kα	PET	apatite	0.01
Pb	Mα	PET	$PbCrO_4$	0.09
Si	Kα	TAP	wollastonite	0.01
Ti	Kα	PET	rutile	0.04
U	Mß	PET	vorlanite	0.07
Y	Lα	TAP	$Y_3Al_5O_{12}$	0.05
Yb	Lα	LiF	REE3	0.10
Zr	Lα	PET	zircon ED2	0.06

The code REE3 refers to glasses containing *REE* (*REE*PO_4) (Jarosewich & Boatner, 1991)

Acceleration voltage 15 kV, probe current 40 nA

Table 11 Analytical conditions for monazite

Element	Line	Crystal	Standard	Approx. detection limit (wt.%)
Ca	Kα	PET	diopside	0.01
Ce	Lα	PET	$CePO_4$	0.06
Dy	Lß	LIF	$DyPO_4$	0.23
F	Kα	TAP	fluorite	0.07
Fe	Kα	LIF	hematite	0.04
Gd	Lß	LIF	$GdPO_4$	0.11
Ho	Lß	LIF	HoP_5O_{14}	0.22
La	Lα	PET	$LaPO_4$	0.07
Mn	Kα	LIF	rhodonite	0.04
Nd	Lß	LIF	$NdPO_4$	0.12
P	Kα	PET	$Ca_5\ P_3\ O_{12}F$	0.03
Pb	Mß	LPET	$PbCrO_4$	0.03
Pr	Lß	LIF	$PrPO_4$	0.12
Si	Kα	TAP	wollastonite	0.02
Sm	Lß	LIF	SmP_5O_{14}	0.11
Th	Mα	PET	ThO_2 synthetic	0.06
U	Mß	LPET	vorlanite	0.02
Y	Lα	TAP	$Y_3Al_5O_{12}$	0.03
Yb	Lα	LIF	REE3	0.13

The code REE3 refers to glasses containing *REE* (*REE*PO_4)

(Jarosewich & Boatner, 1991), other *REEPO₄* glasses were prepared and offered to the lab by dr Daniel Harlov

Acceleration voltage used - 20 kV, probe current - 40 nA

Detailed conditions, used only for chemical dating, are attached in an additional file. Before dating, monazite grains were element mapped (Y) with a Σigma VP Zeiss FE-SEM equipped with two SDD type Bruker XFlash|10 EDS detectors. The relative abundance of Y was determined from the interference-free Y$K\alpha$ line and Y$L\alpha$ deconvolution, but is not present as there is no significant Y variation. The maximum available 30 kV acceleration voltage was used for the most effective generation of Y$K\alpha$ X-rays, but the second largest 60 μm aperture was used to stay below the 25% dead time of the EDS signal processing unit

Table 12 Analytical conditions for thorite

Element	Line	Crystal	Standard	Approx.detection limit (wt.%)
Ca	Lα	PET	$CaSiO_3$	0.03
Ce	Kα	PET	CeP_5O_{14}	0.12
Gd	Lβ	LiF	$Gd_3Ga_5O_{12}$	0.44
La	Lα	PET	LaB_6	0.11
Nd	Lβ	LiF	$NdGaO_3$	0.39
P	Kα	PET	apatite BB2	0.04
Pb	Mα	PET	$PbCrO_4$	0.21
Pr	Lβ	LiF	REE1	0.44
Si	Kα	TAP	wollastonite	0.02
Sm	Lβ	LiF	REE3	0.42
Th	Mα	PET	ThO_2 synthetic	0.25
U	Mβ	PET	vorlanite	0.22
Y	Lα	TAP	$Y_3Al_5O_{12}$	0.06

The codes REE1 to REE3 refer to glasses containing REE ($REEPO_4$) (Jarosewich and Boatner, 1991)

Acceleration voltage 15 kV, probe current 20 nA

FileName: BB-n270116.qtiDat

Signal(s) Used: P Ka, Y La, La La, Ce La, Pr Lb, Nd Lb, Sm Lb, Gd Lb, Dy Lb, Er La, Pb Mb, Ca Ka, Th Ma, U Mb, Si Ka

Spectromers Conditions: Sp1 PET, Sp3 TAP, Sp1 PET, Sp1 PET, Sp2 LIF, Sp2 LIF, Sp2 LIF, Sp2 LIF, Sp2 LIF, Sp2 LIF, Sp4 LPET, Sp1 PET, Sp1 PET, Sp4 LPET, Sp3 TAP

Full Spectromers Conditions: Sp1 PET(2d = 8.75,K = 0.000144), Sp3 TAP(2d = 25.745,K = 0.00218), Sp1 PET(2d = 8.75,K = 0.000144), Sp1 PET(2d = 8.75,K = 0.000144), Sp2 LIF(2d = 4.0267,K = 0.000058), Sp2 LIF(2d = 4.0267,K = 0.000058), Sp2 LIF(2d = 4.0267,K = 0.000058), Sp2 LIF(2d = 4.0267,K = 0.000058), Sp2 LIF(2d = 4.0267,K = 0.000058), Sp4 LPET(2d = 8.75,K = 0.000144), Sp1 PET(2d = 8.75,K = 0.000144), Sp1 PET(2d = 8.75,K = 0.000144), Sp4 LPET(2d = 8.75,K = 0.000144), Sp3 TAP(2d = 25.745,K = 0.00218)

Column Conditions: Cond 1: 20 keV 40 nA
Date: 29-Dec-2016
User Name: SX
Setup Name: Mona_PD4A.qtiSet
DataSet Comment: Namaqualand
Comment:
Analysis Date: 1/27/2016 3:14:17 PM
Project Name: Default Project
Sample Name: Default Sample
Analysis Parameters:

Sp	Elements	Xtal	Position	Bg+	Bg-	Slope	Bias	Gain	Dtime	Blin	Wind	Mode
Sp1	P Ka	PET	70,350	-800	1150		1284	859	3	560		Inte
Sp3	Y La	TAP	25,091	-500		1	1270	2381	3	560		Inte
Sp1	La La	PET	30,456	-700	1100		1283	853	3	560		Inte
Sp1	Ce La	PET	29,271	-650	950		1283	853	3	560		Inte
Sp2	Pr Lb	LIF	56,076	-600	800		1804	351	3	560		Inte
Sp2	Nd Lb	LIF	53,800		1700	1.1	1815	356	3	560		Inte
Sp2	Sm Lb	LIF	49,625	-600	500		1813	352	3	560		Inte
Sp2	Gd Lb	LIF	45,859	-750	1820		1806	347	3	560		Inte
Sp2	Dy Lb	LIF	42,462	-695	1150		1803	337	3	560		Inte
Sp2	Er La	LIF	44,305	-1160	1230		1808	349	3	560		Inte
Sp4	Pb Mb	LPET	58,027	-350	1650		1819	802	3	560		Inte
Sp1	Ca Ka	PET	38,390		500	1.1	1286	871	3	560		Inte
Sp1	Th Ma	PET	47,275	-650	700		1282	873	3	560		Inte
Sp4	U Mb	LPET	42,463	-900	1050		1815	787	3	560		Inte
Sp3	Si Ka	TAP	27,731		400	1.1	1270	2381	3	560		Inte

Peak Position: Sp1 70350 (−800, 1150), Sp3 25091 (−500), Sp1 30456 (−700, 1100), Sp1 29271 (−650, 950), Sp2 56076 (−600, 800), Sp2 53800 (1700, 1.1), Sp2 49625 (−600, 500), Sp2 45859 (−750, 1820), Sp2 42462 (−695, 1150), Sp2 44305 (−1160, 1230), Sp4 58027 (−350, 1650), Sp1 38390 (500, 1.1), Sp1 47275 (−650, 700), Sp4 42463 (−900, 1050), Sp3 27731 (400, 1.1)

Standard composition:
Ca5P3O12F = Ca: 39.7368%, P: 18.4251%, O: 38.071%, F: 3.7671%
YPO4 = Y: 48.3501%, P: 16.8446%, O: 34.8053%
LaPO4 = La: 59.392%, P: 13.2435%, O: 27.3645%
CePO4 = Ce: 59.6018%, P: 13.1751%, O: 27.2231%
PrPO4 = Pr: 59.7367%, P: 13.1311%, O: 27.1322%
NdPO4 = Nd: 60.2976%, P: 12.9482%, O: 26.7542%

SmP5O14 = Sm: 28.4166%, P: 29.2609%, O: 42.3225%
GdPO4 = Gd: 62.3455%, P: 12.2803%, O: 25.3742%
DyPO4 = Dy: 63.1133%, P: 12.0299%, O: 24.8568%
ErPO4 = Er: 63.7828%, P: 11.8115%, O: 24.4056%
PbCrO4 = Pb: 64.1098%, Cr: 16.0881%, O: 19.8022%
Diopside-21 = O: 44.3%, Mg: 11.23%, Al: 0.05%, Si: 25.88%, Ca: 18.39%, Ti: 0.05%, Mn: 0.04%, Fe: 0.04%
ThO2 = Th: 87.8806%, O: 12.1194%
UO2 = U: 88.1495%, O: 11.8505%
Calibration file name (Element intensity cps/nA):
P: Ca5P3O12F_P Sp1_P Sp4_001.calDat (P: 81.4 cps/nA)
Y: YPO4_Y Sp3_001.calDat (Y: 403.9 cps/nA
La: LaPO4_LaSp1_LaSp2_LaSp4_001.calDat (La: 287.9 cps/nA)
Ce: CePO4_CeSp1_CeSp2_CeSp4_001.calDat (Ce: 291.8 cps/nA)
Pr: PrPO4_PrSp2_001.calDat (Pr: 38.3 cps/nA)
Nd: NdPO4_NdSp1_NdSp2_NdSp4_001.calDat (Nd: 47.8 cps/nA)
Sm: SmP5O14_SmSp2_001.calDat (Sm: 23.4 cps/nA)
Gd: GdPO4_GdSp2_001.calDat (Gd: 62.6 cps/nA)
Dy: DyPO4_DySp2_001.calDat (Dy: 68.7 cps/nA)
Er: ErPO4_ErSp2_001.calDat (Er: 124.4 cps/nA)
Pb: PbCrO4_PbSp4_001.calDat (Pb: 137.2 cps/nA)
Ca: Diopside-21_CaSp1_CaSp4_001.calDat (Ca: 221.1 cps/nA)
Th: ThO2_ThSp1_ThSp4_005.calDat (Th: 104.6 cps/nA)
U: UO2_U Sp1_U Sp4_005.calDat (U: 462.2 cps/nA)
Si: Diopside_SiSp3_005.calDat (Si: 468.5 cps/nA)
Beam Size: 0 μm

References

Anderson AJ, Wirth R, Thomas R (2008) The alteration of metamict zircon and its role in the remobilization of high-field-strength elements in the Georgeville granite, Nova Scotia. Scotia. Can Mineral 46:1–18

Bagiński B, Macdonald R, Dzierżanowski P, Zozulya D, Kartashov PM (2015) Hydrothermal alteration of chevkinite-group minerals: products and mechanisms. Part 1. Hydration of chevkinite-(Ce). Mineral Mag 79:1019–1037

Bagiński B, Zozulya D, Macdonald R, Kartashov PM, Dzierżanowski P (2016) Low-temperature hydrothermal alteration of a rare-metal rich quartz-epidote metasomatite from the El'ozero deposit, Kola Peninsula. Russia Eur J Mineral 28:789–910

Baltybayev SH, Levchenkov OA, Levsky LK (2009) Svecofenian belt of Fennoscandia: spatial and temporal correlation of early Proterozoic endogenic processes. Nauka, St Petersburg, pp. 328. (in Russian)

Bayanova TB (2004) The age of reference geological complexes of the Kola region and duration of magmatic processes. Nauka, St Petersburg, pp 174. (in Russian)

Bayanova TB, Voloshin AV (1999) U-Pb dating of zircon megacrysts (8 cm) from amazonite-rand-pegmatite of Mt. Ploskaya, Baltic shield. EUG-10 abstracts, Strasbourg, p 153

Bel'kov IV, Batieva ID, Vinogradova GV, Vinogradov AN (1988) Mineralization and fluid regime in the contact zones of alkali granite intrusions. Kola branch, USSR. Academy of Sciences, Apatity, pp 110. (in Russian)

Berger A, Gnos E, Janots E, Fernandez A, Giese J (2008) Formation and composition of rhabdophane, bastnäsite and hydrated thorium minerals during alteration: implications for geochronology and low-temperature processes. Chem Geol 254:238–248

Bosse V, Boulvais P, Gautier P, Tiepolo M, Ruffet G, Devidal JL, Cherneva Z, Gerdjikov I, Paquette JL (2009) Fluid-induced disturbance of the monazite Th-Pb chronometer: in situ dating and element mapping in pegmatites from the Rhodope (Greece, Bulgaria). Chem Geol 261:286–302

Broska I, Petrík I, Williams CT (2000) Coexisting monazite and allanite in peraluminous granitoids of the Tribeč Mountains, western Carpathians. Am Mineral 85:22–32

Budzyń B, Hetherington CJ, Williams MI, Jercinovic MJ, Michalik M (2010) Fluid- mineral interactions and constraints on monazite alteration during metamorphism. Mineral Mag 74:659–681

Budzyń B, Harlov DE, Williams ML, Jercinovic MJ (2011) Experimental determination of stability relations between monazite, fluorapatite, allanite, and REE-epidote as a function of pressure, temperature, and fluid composition. Am Mineral 96:1547–1567

Drysdall AR, Jackson NR, Ramsay CR, Hackett D (1984) Rare element mineralization related to Precambrian alkali granites in the Arabian shield. Econ Geol 79:1366–1377

Ercit TS (2005) Identification and alteration trends of granitic-pegmatite-hosted (Y,REE,U,Th)-(Nb,Ta,Ti) oxide minerals: a statistical approach. Can Mineral 43:1291–1303

Ervanne H (2004) Uranium oxidation states in allanite, fergusonite and monazite of pegmatites from Finland. N Jahr Mineral Mon 2004: 289–301

Förster H-J (1998) The chemical composition of REE-Y-Th-U-rich accessory minerals in peraluminous granites of the Erzegebirge-Fichtelgebirge region, Germany, part 1: the monazite-(Ce)-brabantite solid solution series. Am Mineral 83: 259–272

Geisler T, Rashwan AA, Rahn MKW, Poller U, Zwingmann H, Pidgeon RT, Schleicher H, Tomaschek F (2003a) Low-temperature hydrothermal alteration of natural metamict zircon from the Eastern Desert, Egypt. Mineral Mag 67:485–508

Geisler T, Trachenko K, Rios S, Dove MT, Salje EKH (2003b) Impact of self-irradiation damage on the aqueous durability of zircon ($ZrSiO_4$): implications for its suitability as a nuclear waste form. J Phys Condens Matter 15:L597–L605

Gieré R, Williams CT, Wirth R, Ruschel K (2009) Metamict fergusonite-(Y) in a spessartine-bearing granitic pegmatite from Adamello, Italy. Chem Geol 261:333–345

Gorbatschev R, Bogdanova S (1993) Frontiers in the Baltic shield. In: Gorbatschev, R (ed) the Baltic shield. Spec Vol, Precambrian Res 64:3–21

Harlov DE, Hetherington CJ (2010) Partial high-grade alteration of monazite using alkali-bearing fluids: experiments and nature. Am Mineral 95:1105–1108

Harlov DE, Wirth R, Förster H-J (2005) An experimental study of dissolution- reprecipitation in fluorapatite: fluid infiltration and the formation of monazite. Contrib Mineral Petrol 150:268–286

Harlov DE, Wirth R, Hetherington CJ (2007) The relative stability of monazite and huttonite at 300-900 °C and 200-1000 MPa: Metasomatism and the propagation of metastable mineral phases. Am Mineral 92:1652–1664

Harlov DE, Wirth R, Hetherington CJ (2011) Fluid-mediated partial alteration in monazite: the role of coupled dissolution-reprecipitation in element redistribution and mass transfer. Contrib Mineral Petrol 162:329–348

Hetherington CJ, Harlov DE (2008) Metasomatic thorite and uraninite inclusions in xenotime and monazite from granitic pegmatites, Hidra anorthosite massif, southwestern Norway: mechanics and fluid chemistry. Am Mineral 93:806–820

Hetherington CJ, Harlov DE, Budzyń B (2010) Experimental metasomatism of monazite and xenotime: mineral stability, REE mobility and fluid composition. Mineral Petrol 99:165–184

Jarosewich E, Boatner L (1991) Rare-earth element reference samples for electron microprobe analysis. Geostand Newslett 15:397–399

Jiang N (2006) Hydrothermal alteration of chevkinite-(Ce) in the Shuiquangou syenitic intrusion, northern China. Chem Geol 227:100–112

Johan Z, Johan V (2005) Accessory minerals of the Cínovec (Zinnwald) granite cupola, Czech Republic: indicators of petrogenetic evolution. Mineral Petrol 83:113–150

Kartashov PM (1994) Zr- and Nb-bearing varieties of chevkinite-(Ce) and their alteration products, first occurrence in Mongolia. Ninth IAGOD Symp (Beijing) 2:696–697

Kartashov PM, Voloshin AV, Pakhomovsky YA (1993) On the zonal gadolinite from the alkaline granitic pegmatites of Haldzan-Buragtag (Mongolian Altai). Proc Russ mineral Soc 1993, Nr 3: 65–79. (in Russian)

Lisowiec K, Budzyń B, Słaby E, Renno AD, Götze J (2013) Fluid-induced magmatic and post-magmatic zircon and monazite patterns in granitoid pluton and related rhyolitic bodies. Chem Erde 73:163–179

Lumpkin GR, Smith KL, Gieré R, Williams CT (2004) Geochemical behaviors of host phases for actinides and fission products in crystalline ceramic nuclear waste forms. In: Gieré R, Stille P (eds) energy, waste and the environment: a geochemical perspective: Geol Soc, London, Spec Pub 236:89–111

Lumpkin GR, Gao Y, Gieré R, Williams CT, Mariano AN, Geisler T (2014) The role of Th-U minerals in assessing the performances of nuclear waste forms. Mineral Mag 78:1071–1097

Lyalina LM, Zozulya DR, Savchenko YE, Tarasov MP, Selivanova EA, Tarasova E (2014) Fluorbritholite-(Y) and yttrialite-(Y) from silexites of the Keivy alkali granites, Kola Peninsula. Geol Ore Dep 56:589–602

Macdonald R, Belkin HE, Wall F, Bagiński B (2009) Compositional variation in the chevkinite group: new data from igneous and metamorphic rocks. Mineral Mag 73:777–796

Macdonald R, Bagiński B, Kartashov P, Zozulya D, Dzierżanowski P (2012) Chevkinite-group minerals from Russia and Mongolia: new compositional data from fenites, metasomatites and ore deposits. Mineral Mag 76:535–549

Macdonald R, Bagiński B, Kartashov PM, Zozulya D, Dzierżanowski P (2015a) Hydrothermal alteration of chevkinite-group minerals. Part 2. Metasomatite from the Keivy massif, Kola Peninsula, Russia. Mineral Mag 79:1039–1059

Macdonald R, Bagiński B, Kartashov PM, Zozulya D, Dzierżanowski P (2015b) Interaction of rare-metal minerals with hydrothermal fluids: evidence from quartz-epidote metasomatites of the Haldzan massif, Mongolian Altai. Can Mineral 53:1015–1034

Macdonald R, Bagiński B, Kartashov PM, Zozulya D, Dzierżanowski P, Jokubauskas P (2015c) Hydrothermal alteration of a chevkinite-group mineral to a bastnäsite-(Ce)-ilmenite-columbite-(Fe) assemblage: interaction with a F-, CO_2-rich fluid. Mineral Petrol 109:659–678

Meldrum A, Wang LM, Ewing RC (1996) Ion-beam-induced amorphization of monazite. Nucl Instrum Methods B 116:220–224

Meldrum A, Boatner LA, Wang LM, Ewing RC (1997) Displacive radiation effects in the monazite- and zircon-structure orthophosphates. Phys Rev B56:13805–13814

Meldrum A, Boatner LA, Ewing RC (2000) A comparison of radiation effects in crystalline ABO_4-type phosphates and silicates. Mineral Mag 64:185–194

Mitrofanov FP, Zozulya DR, Bayanova TB, Levkovich NV (2000) The world's oldest anorogenic alkali granitic magmatism in the Keivy structure on the Baltic shield. Dokl Earth Sci 374:1145–1148

Nasdala L, Kronz A, Wirth R, Váczi T, Pérez-Soba C, Willner A, Kennedy AK (2009) The phenomenon of deficient electron microprobe totals in radiation-damaged and altered zircon. Geochim Cosmochim Acta 73:1637–1650

Nasdala L, Hanchar JM, Rhede D, Kennedy AK, Váczi T (2010) Retention of uranium in complexly altered zircon: an example from Bancroft, Ontario. Chem Geol 269:290–300

Ondrejka M, Uher P, Putiš M, Broska I, Bačík P (2012) Two-stage breakdown of monazite by post-magmatic and metamorphic fluids: an example from the Veporic orthogneiss, western Carpathians, Slovakia. Lithos 142-143:245–255

Pérez-Soba C, Villaseca C, Gonzáles del Tánago J, Nasdala L (2007) The composition of zircon in the peraluminous Hercynian granites of the Spanish central system batholith. Can Mineral 45:509–527

Poitrasson F, Chenery S, Shepherd TJ (2000) Electron microprobe and LA-ICP-MS study of monazite hydrothermal alteration: implications for the U-Th-Pb geochronology of nuclear ceramics. Geochim Cosmochim Acta 64:3283–3297

Pouchou JL, Pichoir JF (1991) Quantitative analysis of homogeneous or stratified microvolumes applying the model 'PAP'. In: Newbury H (ed) Electron probe quantitation. Plenum Press, New York, pp 31–75

Prol-Ledesma R-M, Melgarejo JC, Martin RF (2012) The el Muerto "NYF" granitic pegmatite, Oaxaca, Mexico, and its striking enrichment in allanite-(Ce) and monazite-(Ce). Can Mineral 50:1055–1076

Rämö OT, Haapala I (1995) One hundred years of Rapakivi granite. Mineral Petrol 52:129–185

Rasmussen B, Muhling JR (2007) Monazite begets monazite: evidence for dissolution of detrital monazite and reprecipitation of syntectonic monazite during low-grade regional metamorphism. Contrib Mineral Petrol 154:675–689

Ruschel K, Nasdala L, Rhede D, Wirth R, Lengauer CL, Libowitsky E (2010) Chemical alteration patterns in metamict fergusonite. Eur J Mineral 22:425–433

Seydoux-Guillaume A-M, Paquette JL, Wiedenbeck M, Montel JM, Heinrich W (2002) Experimental resetting of the U-Th-Pb system in monazite. Chem Geol 191:165–181

Seydoux-Guillaume A-M, Wirth R, Ingrin J (2007) Contrasting response of $ThSiO_4$ and monazite to natural irradiation. Eur J Mineral 19:7–14

Seydoux-Guillaume A-M, Montel J-M, Bingen B, Bosse V, de Parseval P, Paquette J-L, Janots E, Wirth R (2012) Low-temperature alteration of monazite: fluid mediated coupled dissolution-precipitation, irradiation damage, and disturbance of the U-Pb and Th-Pb chronometers. Chem Geol 330-331:140–158

Skridlaite G, Bogdanova S, Taran L, Bagiński B (2014) Recurrent high grade metamorphism recording a 300 ma long Proterozoic crustal evolution in the western part of the east European craton. Gondwana Res 25:649–667

Smith DGW, de St. Jorre L, Reed SJB, Long JVP (1991) Zonally metamictised and other zircons from Thor Lake, northwest territories. Can Mineral 29:301–309

Sun S-S, McDonough WF (1989) Chemical and isotopic systematics of oceanic basalts: implications for mantle composition and processes. In: Saunders AD, Norry M J (eds), magmatism in the ocean basins. Geol Soc Lond Spec Publ 42:313–345

Tomašíc N, Gajović A, Bermanec V, Su DS, Rajić Linarić M, Ntaflos T, Schlögl R (2006) Recrystallization mechanisms of fergusonite from metamict mineral precursors. Phys Chem Miner 33:145–159

Uher P, Ondrejka M, Konečny P (2009) Magmatic and post-magmatic Y-*REE*-Th phosphate, silicate and Nb-ta-Y-*REE* oxide minerals in A-type metagranite: an example from the Turčok massif, the western Carpathians, Slovakia. Mineral Mag 73:1009–1025

Utsunomiya S, Valley JW, Cavosie AJ, Wilde SA, Ewing RC (2007) Radiation damage and alteration of zircon from a 3.3 Ga porphyritic granite from the Jack Hills, Western Australia. Chem Geol 236:92–111

Van Lichtervelde M, Melcher F, Wirth R (2009) Magmatic *vs*. hydrothermal origins for zircon associated with tantalum mineralization in the Tanco pegmatite, Manitoba, Canada. Am Mineral 94:439–450

Vlach SRF, Gualda GAR (2007) Allanite and chevkinite in A-type granites and syenites of the Graciosa Province, southern Brazil. Lithos 97:98–121

Watt GR (1995) High-thorium monazite-(Ce) formed during disequilbrium melting of metapelites under granulite-facies conditions. Mineral Mag 59:735–743

Williams ML, Jercinovic MJ, Harlov DE, Budzyń B, Hetherington CJ (2011) Resetting monazite ages during fluid-related alteration. Chem Geol 283:218–225

Zozulya D, Eby GN (2010) Rare-metal ore occurrences, related to the late Archean A- type granites from the Keivy zone (NE Fennoscandian shield). In: Ramo OT, Lukkari SR, Heinonen AP (eds) international conference on A-type granites and related rocks through time (IGCP-510). Helsinki, Finland, august 18-20. Abstract volume, pp 113-115

Zozulya DR, Bayanova TB, Eby GN (2005) Geology and age of the late Archean Keivy alkaline province, northeastern Baltic shield. J Geol 113:601–608